SOLAR EQUILIBRIUM À LA GRAD-SHAFRANOV

LEE MICHAEL GUNDERSON

A DISSERTATION

PRESENTED TO THE FACULTY

OF PRINCETON UNIVERSITY

IN CANDIDACY FOR THE DEGREE

OF DOCTOR OF PHILOSOPHY

RECOMMENDED FOR ACCEPTANCE

BY THE DEPARTMENT OF

ASTROPHYSICAL SCIENCES

PROGRAM IN PLASMA PHYSICS

ADVISOR: AMITAVA BHATTACHARJEE

SEPTEMBER 2020

Abstract

This dissertation investigates the extent to which features of the solar interior can be described by magnetohydrodynamic equilibria. Essentially, we solve the generalized Grad–Shafranov equation, with observational constraints serving as (incomplete) boundary conditions, thereby offering a family of plausible internal solar profiles.

Numerical simulations can offer insight into the interior dynamics and help identify which ingredients are necessary to reproduce particular observations. However, they are computationally intensive; fully resolved simulations of the solar interior will likely remain hypothetical for several solar cycles. Fortunately, despite being rife with turbulence, many features of the Sun can be understood analytically from an equilibrium perspective (e.g., Parkers laminar model of the supersonic solar wind).

To help identify which features admit an equilibrium description, we analyze stationary axisymmetric ideal magnetohydrodynamic flows for solar-relevant parameters. Our numerical scheme for obtaining global solutions uses the Lagrangian formulation of the resulting generalized Grad–Shafranov equation, employing a novel method for incorporating unconstrained boundary conditions (Chapter 3).

Beginning with the outer layers of the Sun, we show that the hydrodynamic limit is sufficient to describe the observed deviation from the cylindrical rotation in the solar Convection Zone (Chapter 4). Moreover, the inclusion of a poloidal flow results in a slowing of rotation at the surface, qualitatively similar to the Near Surface Shear Layer (Chapter 5).

Turning inward, we then investigate the effects of including a magnetic field, and its relationship to the Tachocline and the Radiative Interior (Chapter 6). The presence of both a poloidal field and poloidal flow can result in the equilibrium equations transitioning to hyperbolic type, and could lead to discontinuities or steep gradients characteristic of the Tachocline. While observations at the solar surface indicate that these transitions occur

suggestively close to the Tachocline, we find that there exist solutions that remain smooth throughout, though they might not be robust to perturbations.

Coupled with the increasing sensitivity of extraterrestrial seismic and magnetic measurements, our framework could offer plausible extrapolations into the hidden interiors of other astrophysical objects, helping to determine which features have an equilibrium description, and which are necessarily dynamical in origin.

Acknowledgements

My parents, for making me. My wife's parents, for making her. The DBar, for introducing me to her. And her, Gecia Bravo-Hermsdorff, for being my main collaborator, both in life and academia, fighting by my side in every battle, both emotional and cognitive. Our canine offspring, Ashlyn Maria Grav, for accompanying me when I needed to be let outside.

My PPPL cohort: Jacob Schwartz, Charles Swanson, Jonathan Ng, Peter Bolgert, Yuan Shi, and Daniel Ruiz. My advisor, Amitava Bhattacharjee, for support, insight, advice, and patience. Matt Kunz, for detailed feedback on this manuscript. Stuart Hudson, for sharing his numerical intuition with me through a variety of colorful parables and metaphors. Hong Qin and James Stone, for serving on my thesis committee. Manasvi Lingham, for insightful conversations while circling the PPPL campus, as well as two of the best book recommendations I have ever received. Chris Smiet, for highly enjoyable topological conversations. And all the other amazing people I've had the pleasure to meet at PPPL.

My PNI quasi-cohort: Alex Piet, Talmo Pereira, Matt Panichello and Olga Lositsky, Alex Song and Diana Liao, Ben Deverett, Luis Piloto, Jamal Williams, Kim Stachenfeld, Bas van Opheusden. Other members of my Princetonian family: Matt Hernandez, Matthew de Courcy-Ireland, Farzan Beroz, Jersey Transit, Zach Sethna, Felicity Hills, Daniel Vitek, Shai Chester. Other members of my "extended" family: Livia Camargo, Joe Olson, Aurelio Amaral, Bruno Pace.

Thank you all.

To my strange loop, Gecia Bravo-Hermsdorff.

Contents

Chapter 1

Physics of the Solar Interior:

A Historical Overview

You do not beg the Sun for mercy.

—— Frank Herbert, *Dune Messiah*

1.1 A Copernican Corollary

The Sun is a rather unremarkable G-type star. However, indulging an anthropocentric viewpoint, the Sun is in the unique position of being orders of magnitude closer to the Earth than any other star, a fact of epistemological relevance. Indeed, over the course of its close relationship with humanity, we have come to discover many surprising aspects of its personality.

1.2 The pedagogical value of sunspots

Far from being an immaculate sphere of the heavens, the Sun is close enough to reveal its imperfections. Sunspots have been observed since antiquity, the earliest known record being from the Chinese Book of Changes, c 800 BCE[1] [108]. The earliest known drawing appears much later, in 1128, by John of Worchester [102] (see Figure 1.1 for his artistic abilities).

Figure 1.1: **Earliest known drawing of sunspots, by John of Worchester in AD 1128, December 8.** About five days later, associated geomagnetic storms were seen in regions remarkably far from the poles, with multiple Korean and Chinese written records (image taken from [102]).

With the aid of telescopes and systematic observations, in the early 15$^{\text{th}}$ century, Giordano Bruno and Johannes Kepler posited that the spots were not orbiting objects, and were in fact surface features. Furthermore, they suggested that the systematic movement of these spots from west to east indicated that the Sun rotates about its axis. Thereafter, there were many attempts to use sunspots to infer the rotation rate of the Sun, arriving at reasonable estimates on the order of a month. However, the variations in these results were not particu-

[1]The author agrees with the sentiment of the footnote on page xv of [20], viz, omitting superfluous full stops to obtain a more efficient compression of, eg: *videlicet*, *exempli gratia*, etc.

larly well-understood. It was not until the middle of the 19th century that these blemishes were noticed to come in cycles [87] (Figure 1.2a), and move faster near the equator [17] (Figure 1.2b).

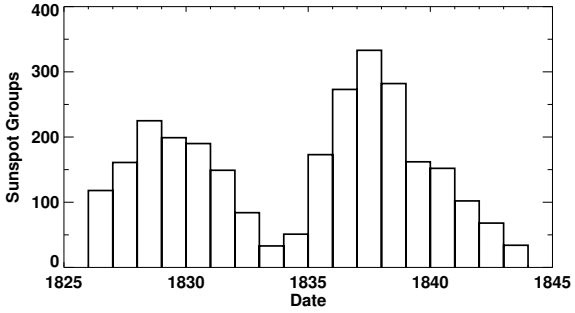

Latitude.	Daily Drift.					
30° N	− 25′	in longitude	+ 5′	in latitude, by	4	series
18 N	− 14	..	+ 1	..	4	..
8 N	+ 8	..	− 5	..	14	..
11 S	+ 10	..	− 3	..	6	..
19 S	− 10	..	+ 1	..	5	..
29 S	− 21	..	+ 4	..	8	..

Figure 1.2: **The first systematic studies of sunspots led to the discovery of the solar cycle and latitudinal differential rotation. a)** Data collected by Schwabe, which led to the discovery of the solar cycle [87] (image taken from [51]). **b)** Summary of data from Carrington's studies of sunspot velocity as a function of latitude, which led to the discovery that the equator rotates faster than the poles [17].

1.3 The Doppler discrepancy

Tracking sunspots only gets one so far, and the advent of doppler measurements provided a more direct method for observing our Dizzy Deity. Around the end of the 19th century, measurements of the solar surface velocity confirmed that the surface of the Sun exhibits the same differential rotation, albeit notably slower [23]. As doppler measurements improved, it became definitively clear that sunspots were consistently rotating faster than the surrounding photosphere [101]. During this time, sunspots also received the first astrophysical application of the Zeeman effect, when Hale presented evidence of their magnetic origin [47]. The

suggestion that these magnetic features were anchored to more rapidly rotating subsurface layers marked one of the first (correct) inferences about the interior rotation of the Sun [30].

1.4 Helioseismology

By the middle of the 20$^{\text{th}}$ century, it was clear that radiative diffusion was insufficient to transport the energy from the fusing core to the surface, and that the outer layers of the Sun were convectively unstable [106]. Much in the same way that details about the terrestrial interior are inferred by observing how earthquakes bounce off the inside of the Earth [91], the dynamics of such convection-induced "sunquakes" were suggested as a way to indirectly probe the solar interior [38].

Fortunately, the Sun is effectively "quaking" all the time; supersonic convection at the solar surface generates sound waves, which then propagate throughout the interior, setting up global standing modes. Through high-resolution Doppler measurements of the resulting motion of the solar surface, it is possible to resolve hundreds of thousands of unique frequencies at which the Sun resonates. These different frequencies are associated with different eigenfunctions, which sample different spatial regions of the Sun. The challenge (taken up by helioseismology) is then to solve the formidable inverse problem of finding a plausible internal solar profile that has these frequencies as its spectrum. The growth in complexity of helioseismology can be segmented into a sort of scientific trilogy: ordered by decreasing amount of assumed symmetry (which, unsurprisingly, is also their chronological order).

1.4.1 Spherical helioseismology

We call the first act "spherical" helioseismology, as it treats the Sun as a spherically symmetric ball of gas.

Under this spherical assumption, the frequencies can be interpreted as eigenvalues of the wave equation in spherical coordinates, but with a sound speed that changes as a function of radius. The inverse problem is then to find an appropriate radial profile for the sound speed, such that the resulting eigenvalues match these observed frequencies (see Figure 1.3). After some regularization, a plausible profile can be found. Newton's gravitational law, the hydrostatic assumption, and some knowledge of the appropriate equation of state, can then be leveraged to back out the density, pressure, and entropy as a function of radius. It is the abrupt flattening of this radial entropy profile at around 70 percent of the radius that provided the first accurate measurement of the depth of the solar convection zone (see Figure 6.2 and Chapter 4).

While spherical symmetry is a reasonable lowest-order approximation, the Sun does indeed have a preferred direction, namely that of its rotation axis.

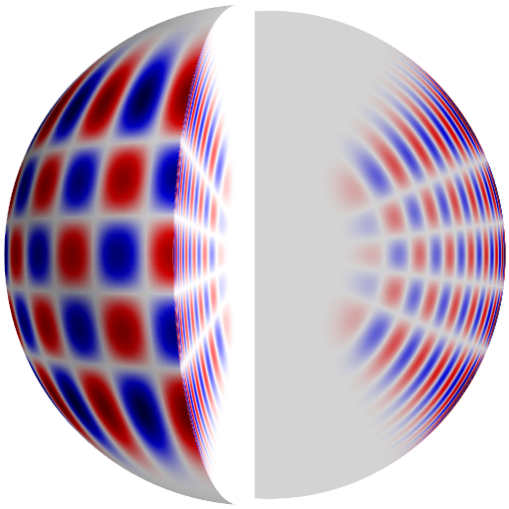

Figure 1.3: **Example of the spatial profile of a standing solar sound wave.** Illustration of an eigenfunction of the spherical wave equation (radial order $n = 14$, angular degree $l = 20$ and azimuthal order $m = 16$), where the sound speed as a function of radius is given by a standard solar model [22]. Colors denote radial displacement. The low amplitude in the deep interior and near the poles results in an insensitivity to the behavior in these regions.

1.4.2 Cylindrical helioseismology

This leads us to the second act: "cylindrical" helioseismology, so-called due to the assumption that the Sun is rotationally symmetric only about a single preferred axis.

Recall that, in the spherical case, the angular parts of the eigenfunctions (the spherical harmonics) have a degeneracy — either choice of sign for the azimuthal wavenumber m gives the same eigenvalue. As the Sun is only weakly rotating, the eigenfunctions and associated eigenvalues of this system will be very similar to those in the spherically symmetric case.

The key difference is that when rotation is included, the Doppler effect due to toroidal flows[2] serve to upshift the prograde modes, and likewise downshift the retrograde modes.

As the precision of surface Doppler measurements increased, the splitting of these prograde and retrograde modes allowed for an accurate estimation of the internal rotation profile, now as a function of both radius and latitude due to the relaxed symmetry assumption [95, 26] (see Figure 1.4).

While the radial shear in the outer layers due to a slower rotating surface was somewhat expected (Section 1.3), the appearance of a sharp radial gradient at the base of the convection zone came as a relative surprise. We remark that this method is effectively insensitive to the solar poloidal flows.

1.4.3 Local helioseismology

As with any good plot, the final act comes with a twist, discarding all assumptions of symmetry. Due to its ability to probe flows in arbitrary directions, as well as at particular locations in time and space, the final act has been coined "local" helioseismology.

[2]This Doppler effect is different than that used to infer surface velocities. The surface motions are measured via a shift in the electromagnetic frequency, while the internal flows modify the standing sound waves.

In contrast to the first two acts, the protagonist no longer considers global modes of oscillation. Instead, one considers perturbations at one point on the surface, and measures the correlation with subsequent perturbations at some other location. A perturbation at the first point excites sound waves in all directions. As the sound speed increases with depth in the Sun, these wave packets are refracted and bend back towards the surface, appearing at another point some distance away and some time later.

Since the sound speed profile as function of radius is well-characterized by spherical helioseismology, ray-tracing can be used to estimate these waves' trajectories. Again, in the spherically symmetric case, one would expect the transit time from the first point to the second to be equivalent to the reverse. However, if there is a net subsurface flow in the direction from the first to the second point, then the Doppler effect will cause a wave traveling in this direction to arrive earlier than expected. Likewise, the wave traveling in the opposite direction will arrive later than expected. By measuring the splitting of the transit times for waves with trajectories of different directions and depths of penetration, it is possible to determine the poloidal flow as a function of radius and latitude. Moreover, by not integrating over the entirety of the Sun, one can probe the asymmetric motions of large-scale convection.

We note that this method is most accurate near the surface, but becomes quite noisy as the bottom of the convection zone is approached. Moreover, it is relatively insensitive to radial flows, as their contributions to the transit time approximately cancel.

1.5 Differential rotation profile of the solar interior

Arguably, the most beautiful and surprising picture from this general endeavor comes from cylindrical helioseismology, namely, the differential rotation profile of the solar interior.

As shown in Figure 1.4, there are broadly two regions: an outer convection zone, and a radiative interior. The convection zone, so-called because heat transport is dominated by convection, occupies the outer $\sim 30\%$, and is characterized by an equator that rotates faster than the poles. The isorotation contours in this region are consistently tilted with respect to the rotation axis, being approximately radial at mid-latitudes. The radiative interior, so-called because it transports heat primarily by radiative diffusion (as it is stably stratified), lies below the convection zone, and exhibits markedly uniform rotation.

Moreover, as interesting phenomena often arise at boundaries, the interfaces are also given names. The interface between the convection zone and the solar wind is known as the near shear surface layer (NSSL), occupying the outer $\sim 5\%$, and is characterized by a slowing of rotation near the surface. The interface between the radiative interior and the convection zone is known as the tachocline, and corresponds to the surprisingly sharp transition from the interior uniform rotation to the outer differential rotation.

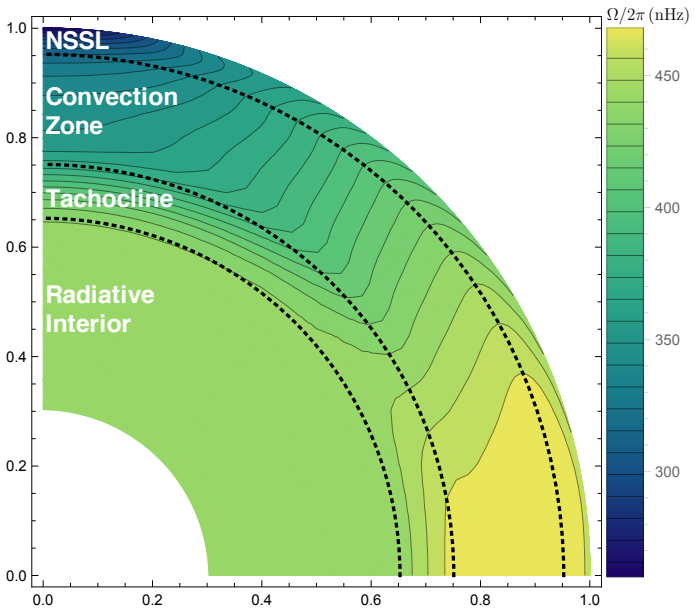

Figure 1.4: **Helioseismology probes the interior of the Sun.** Displayed are contours of constant solar rotation (data from [55]), with lighter colors indicating faster rotation. There are roughly four regions (from interior to surface): the radiative interior, the tachocline, the convection zone (CZ), and the near surface shear layer (NSSL). The radiative interior corresponds to the inner $\sim 70\%$ of the Sun, and is characterized by markedly uniform rotation throughout. The tachocline corresponds to the surprisingly narrow (unresolved) transition from this uniform rotation to the differential rotation of the CZ, where the equator rotates faster than the poles. The NSSL corresponds to the systematically slower rotation in the outer $\sim 5\%$ of the Sun. Note that the inversion kernels used to determine this profile are rather insensitive to the rotation in the deep interior and near the rotation axis, so the relative error in these regions becomes of order unity.

Throughout this thesis, we will discuss some of the open questions about each of these regions. For example, do the gross features of rotation and circulation in the CZ require magnetic fields [73, 74], or does an HD explanation suffice? How important are convective motions for the NSSL [68, 54]? Can the tachocline be understood from an equilibrium perspective, or must turbulence be invoked [90]? Does the tachocline require magnetic fields [39], and if so, can it exist without a solar cycle [11]? To what extent can torsional oscillations be understood as a series of quasi-static equilibria [79, 45]? To help shed light

on some of these questions, which have been considered extensively in the literature, in this thesis, we use the generalized G–S framework to study solar-like equilibrium states. This framework can serve as a "null model" to help determine which features have an equilibrium description, and which are necessarily dynamical in origin.

1.6 Thesis roadmap

The structure of this thesis is as follows. In Chapter 2, we motivate our equilibrium approach and give the relevant equations, namely, those of the Generalized Grad–Shafranov equation. In Chapter 3, we detail our numerical scheme to solve this equation, which uses the Lagrangian formulation and employs a novel method for incorporating unconstrained boundary conditions.

We then present our results for the regions of the Sun. In Chapter 4, we consider the convection zone, showing that the hydrodynamic limit is sufficient to describe the observed deviation from the cylindrical rotation of Taylor–Proudman balance. In Chapter 5, we consider the near surface shear layer, showing that the inclusion of a weak poloidal flow in this hydrodynamic limit results in a qualitative near surface shear layer (albeit smaller). In Chapter 6, we consider the tachocline, showing that there exist smooth solutions crossing the Alfvén surface, although they might not be robust to perturbations.

In Chapter 7, we summarize our results, discuss some caveats of our framework, and outline future directions.

Chapter 2

An Equilibrium Approach

Entities should not be multiplied without necessity.

—— William of Ockham

In this chapter, we describe our theoretical framework. We start by motivating why using an equilibrium model to describe the Sun, a turbulent spheroid, can be a fruitful endeavor (Sections 2.1 and 2.2). We then present the generalized Grad–Shafranov equation (which describe such equilibria), reviewing its derivation and its equivalent Lagrangian formulation (Sections 2.3 and 2.4).

2.1 The surprising insights of stationary solar wind models

The Sun is a complex dynamic turbulent system, with timescales ranging from ~ 10 min for convection, to ~ 10 yr for the solar cycle. Yet, to gain some understanding of its basic behavior, in this thesis, we turn to a relatively simple model: stationary, axisymmetric, ideal

MHD (with arbitrary flows), ie, the generalized Grad–Shafranov equation. Before losing our (justifiably) skeptical reader, we remark that equilibrium models can yield valuable insight, even when applied to markedly non-stationary systems. To support this viewpoint, we now shoehorn a second trilogy into this thesis: that of the surprising success of stationary solar wind models.

2.1.1 The 1D hydrodynamic model of Parker

The solar wind is arguably one of the best examples of well-developed MHD turbulence. However, with only a laminar, spherically symmetric hydrodynamic model, Parker [71] was able to correctly conclude that the solar system is filled with the Sun's supersonic outflow, with the gravitational potential serving as a sort of "de Laval nozzle" [2] for the hot solar atmosphere. While Parker's conclusion was initially not well-received, his qualitative result has since been unambiguously validated [80]. Moreover, his quantitative estimates ($500 - 1500$ km/s) were not far off the mark.

2.1.2 The 1D hydromagnetic model of Weber & Davis

A decade later, Weber & Davis [98] extended the Parker model by including a magnetic field. While still spherically symmetric, their 1D MHD generalization pointed to the importance of the Alfvén radius for solar spin down. Inside this radius, magnetic forces dominate, so the field lines are primarily radial, and the wind co-rotates with the star. Outside this radius, inertial forces dominate, and the field lines form the familiar Parker spiral, with the flow now effectively free streaming. Thus, the effect of the magnetic field is essentially to provide a longer lever-arm so that the star can more effectively shed its angular momentum.

2.1.3 The 2D hydromagnetic model of Sakurai

This spherically symmetric MHD model can be generalized into one that assumes only cylindrical symmetry [70, 53]. This allows one to model the spatial structure of such stellar outflows. In particular, Sakurai [86] found that the critical surfaces are generally shifted to become more prolate, with flows asymptotically aligning with the rotation axis at large spherical radius. Similar results, including cases with a "dead zone" (ie, closed field lines near the equator), were found by Keppens & Goedbloed [58].

2.2 The Great Success of G–S

The equations that govern such 2D hydromagnetic outflows are collectively known as the generalized Grad–Shafranov (G–S) equation, and have a remarkable pedigree of applications. Here, we review some of these applications.

Plasma physicists often first learn about the G–S equation within the context of axisymmetric magnetic confinement devices, in which inertial forces due to flows are negligible. In fact, the magnetostatic version was originally derived in the 1950s to model such experiments [40]. Even now, the design of tokamaks is often guided by this magnetostatic equation and its associated stability analysis, despite the fact that such plasmas are fraught with turbulence, often develop significant rotation, and do not strictly satisfy the assumptions of MHD in the first place (eg, with respect to collisional timescales).

The observation of a toroidal rotation [52] in these experiments motivated the inclusion of flows. Although adding a toroidal flow to the magnetostatic G–S equation results in an extra term in the PDE, it yields no fundamental difference to its properties [96]. The inclusion of a poloidal flow, however, can result in significant qualitative changes. For example, the numerical solutions of Guazzotto et al. [42] suggested that poloidal flows could

be important for internal transport barriers. In particular, as the poloidal flow becomes on the order of the poloidal sound speed $c_{\rm sp} = c_{\rm s} B_{\rm p}/B$, the density can jump discontinuously across flux/stream surfaces. This leads to large shear, potentially suppressing turbulence. While such a transonic equilibrium was later shown to be likely suppressed by resonant interactions [15], the parameter space is quite large, and searching for other ways to exploit peculiarities associated with the poloidal flow may still prove to be a fruitful endeavor.

The G–S equation has also seen a variety of other astrophysical applications, aside from the previously mentioned solar wind. For example, various generalizations have extended its range of applications: relativistic [63, 36, 14] and 2-fluid [92] effects have been included for modeling accretion disks, and superconductivity [61, 60] has been included for neutron stars. One particularly relevant application is its use in reconstructing coherent 2D features *within* the solar wind, using data from only a single flyby of a spacecraft. Essentially, when a spacecraft intercepts a structure in the solar wind, one only obtains data along its 1D trajectory through the full 3D structure [88]. When the structure can be assumed to be elongated, then one can apply the translationally invariant G–S equation to reduce the system to a 2D problem. The data from the spacecraft can then be seen as a sort of "internal boundary condition", and the solution can be integrated (with an appropriate regularization) throughout the entire 2D domain. It is quite remarkable that this process results in a reasonable estimate of the structure, as if it were encoded as a "hologram" in this the lower-dimensional input data. As the mean quantities of the Sun are rotationally symmetric, the equilibrium problem can be similarly reduced to a 2D G–S equation. As observational data are best known near the surface, an analogous inward extrapolation could similarly provide plausible profiles.

Given the success of the G–S equation in providing plausible equilibrium models from incomplete observational data, we propose an application to another compact astrophysical object, the Sun.

2.3 Derivation of the Grad–Shafranov equation

In this section, we outline the derivation of the G–S equation for an axisymmetric plasma with flows in a gravitational potential.

2.3.1 Constructing the flux/stream surfaces

Our starting point is the equation of stationary, axisymmetric, ideal MHD:

$$\underline{\nabla} \cdot (\rho \underline{\mathbf{v}}) = 0, \tag{2.1}$$

$$\underline{\nabla} \cdot \underline{\mathbf{B}} = 0, \tag{2.2}$$

$$\rho \underline{\mathbf{v}} \cdot \underline{\nabla} \underline{\mathbf{v}} + \underline{\nabla} p + \rho \underline{\nabla} \Phi = (\underline{\nabla} \times \underline{\mathbf{B}}) \times \underline{\mathbf{B}}, \tag{2.3}$$

$$\underline{\nabla} \times (\underline{\mathbf{B}} \times \underline{\mathbf{v}}) = \underline{\mathbf{0}}, \tag{2.4}$$

$$\underline{\mathbf{v}} \cdot \underline{\nabla} \sigma = 0, \quad \sigma \equiv \ln \left(p / \rho^{\gamma} \right), \tag{2.5}$$

$$\frac{\partial}{\partial \phi} = 0, \tag{2.6}$$

where ρ, $\underline{\mathbf{v}}$, $\underline{\mathbf{B}}$, p, σ, and Φ are the density, fluid velocity, magnetic field, pressure, entropy, and external potential, respectively, and we have absorbed the permeability into the units of the magnetic field.

Note that, while we close the system by assuming conservation of entropy (equation (2.5)), other choices are also possible. For example, for magnetic confinement experiments, as heat transport along field lines is significantly more efficient than advection by poloidal flows, one might desire a closure that ensures constant temperature along the field lines. This leads to a similar set of equations that we will not consider here.

We use (r, θ, ϕ) for spherical and (λ, z, ϕ) for cylindrical coordinates, with $\lambda = r \sin \theta$, $z = r \cos \theta$, and ϕ as the longitudinal coordinate, ie, the direction of symmetry about the z-axis.

As the magnetic field and mass flux are axisymmetric (equation (2.6)) and divergenceless (equations (2.1) and (2.2)) vector fields, they each admit a convenient representation in terms of two scalar functions of the poloidal plane, which correspond to their poloidal and toroidal components, namely,

$$\underline{\mathbf{B}} = \underline{\nabla}\phi \times \underline{\nabla}\psi + B_\phi \lambda \underline{\nabla}\phi, \tag{2.7}$$

$$\underline{\mathbf{v}} = \frac{1}{\rho}\underline{\nabla}\phi \times \underline{\nabla}\chi + v_\phi \lambda \underline{\nabla}\phi, \tag{2.8}$$

where ψ and χ are axisymmetric. An application of Faraday's law (equation (2.4)) gives

$$\underline{\mathbf{B}} \times \underline{\mathbf{v}} = \underline{\nabla} f, \tag{2.9}$$

where f is some axisymmetric function.

Dotting equation (2.9) with $\underline{\mathbf{B}}$ yields $\underline{\mathbf{B}} \cdot \underline{\nabla} f = 0$. Likewise, dotting equation (2.9) with $\underline{\mathbf{v}}$ yields $\underline{\mathbf{v}} \cdot \underline{\nabla} f = 0$. Hence, the poloidal components of $\underline{\mathbf{B}}$ and $\underline{\mathbf{v}}$ are aligned with each other and with surfaces of constant f. Thus, as $\underline{\nabla}\psi \parallel \underline{\nabla}\chi \parallel \underline{\nabla} f$, we have that $\psi = \psi(\xi)$, $\chi = \chi(\xi)$, $f = f(\xi)$, and

$$\underline{\mathbf{B}} = \psi' \underline{\nabla}\phi \times \underline{\nabla}\xi + B_\phi \lambda \underline{\nabla}\phi, \tag{2.10}$$

$$\underline{\mathbf{v}} = \frac{\chi'}{\rho}\underline{\nabla}\phi \times \underline{\nabla}\xi + v_\phi \lambda \underline{\nabla}\phi, \tag{2.11}$$

where λ is the cylindrical radius; ϕ is the angle about the axis of symmetry; ξ is a scalar "label" of the flux/stream surfaces; $\psi(\xi)$ and $\chi(\xi)$ are arbitrary functions of this label; and primes denote partial differentiation with respect to ξ.

2.3.2 Six arbitrary flux/stream functions

We have seen that the (arbitrary) functions $\psi(\xi)$ and $\chi(\xi)$ determine the poloidal field and flow, respectively. In fact, there are four additional such functions of ξ that appear in the derivation of the generalized Grad–Shafranov equation.

The first of these can be found by substituting equations (2.10) and (2.11) into equation (2.9):

$$F(\xi)\underline{\nabla}\xi = \frac{1}{\lambda}\left(\psi' v_\phi - \frac{\chi'}{\rho}B_\phi\right)\underline{\nabla}\xi \quad \Longrightarrow \quad F(\xi) = \frac{1}{\lambda}\left(\psi' v_\phi - \frac{\chi'}{\rho}B_\phi\right). \tag{2.12}$$

The next can be obtained from the toroidal component of the momentum equation (2.3):

$$\underline{\mathbf{B}} \cdot \underline{\nabla}\left[\lambda(\psi' B_\phi - \chi' v_\phi)\right] = 0 \quad \Longrightarrow \quad L(\xi) = \lambda(\psi' B_\phi - \chi' v_\phi). \tag{2.13}$$

The following function of ξ requires much less vector calculus:

$$\underline{\mathbf{v}} \cdot \underline{\nabla}\sigma = 0 \quad \Longrightarrow \quad \sigma = \sigma(\xi). \tag{2.14}$$

Equations (2.12) and (2.13) give expressions for the toroidal component of the magnetic field and velocity:

$$B_\phi = \frac{L\psi'/\lambda + \lambda F\chi'}{\psi'^2 - \chi'^2/\rho} \tag{2.15}$$

$$v_\phi = \frac{L\chi'/\rho\lambda + \lambda F\psi'}{\psi'^2 - \chi'^2/\rho}. \tag{2.16}$$

The definition of the last function of ξ gives rise to the magnetic generalization of the Bernoulli equation, and deserves its own subsection.

2.3.3 The Bernoulli equation: an algebraic expression for ρ

Force balance (equation (2.3)) in the direction of the field/flow results in the magnetic generalization of the Bernoulli equation, yielding $H(\xi)$, the last function of ξ:

$$H(\xi) = \frac{1}{2}\frac{\chi'^2}{\rho^2}\frac{|\nabla\xi|^2}{\lambda^2} + \frac{1}{2}\frac{\chi'^2}{\rho^2}\left[\left(\frac{L}{\lambda} + \frac{\lambda\chi' F}{\psi'}\right)\Big/\left(\psi'^2 - \frac{\chi'^2}{\rho}\right)\right]^2 - \frac{1}{2}\frac{\lambda^2 F^2}{\psi'^2} + \frac{\gamma}{\gamma-1}\rho^{\gamma-1}e^{\sigma} + \Phi. \tag{2.17}$$

In general, for a given λ, z, and ξ, there are either 0, 2, or 4 solutions for ρ. At some precise points, neighboring roots will briefly coincide. It is at these points that the numerical method should smoothly switch from one solution to the other. We will discuss this issue in depth in Chapter 6.

2.3.4 Correspondence with physical variables

In certain limits, these functions of ξ have clear physical interpretations (eg, pressure and toroidal flux for magnetostatic configurations). In this generalized case, some functions become intertwined. Nevertheless, some loose connections may be made. Clearly, $\sigma(\xi)$ is the entropy, and $\psi'(\xi)$ and $\chi'(\xi)$ control the poloidal field and flow, respectively. As the generalization of the notion of head in fluid mechanics, $H(\xi)$ corresponds to the total energy of the field/flow. The least intuitive functions are $F(\xi)$ and $L(\xi)$. In the hydrodynamic limit ($\chi'^2/\rho \gg \psi'^2$), $L(\xi)$ corresponds to the angular momentum of the flow and $F(\xi)$ controls the toroidal field, while in the magnetostatic limit ($\chi'^2/\rho \ll \psi'^2$), $F(\xi)$ corresponds to the toroidal flux of the field and $L(\xi)$ controls the toroidal flow.

2.3.5 The G–S equation: a PDE for ξ

Force balance (equation (2.3)) in the direction perpendicular to the field/flow yields the G–S equation, a second-order nonlinear PDE governing ξ:

$$\underline{\nabla}\cdot\left[\left(\psi'^2-\frac{\chi'^2}{\rho}\right)\frac{\underline{\nabla}\xi}{\lambda^2}\right]-\frac{1}{2}\left(\psi'^2-\frac{\chi'^2}{\rho}\right)'\frac{\left|\underline{\nabla}\xi\right|^2}{\lambda^2}$$
$$+\left[\left(\frac{L^2}{2\lambda^2}+\frac{\chi' LF}{\psi'}+\frac{\rho\lambda^2F^2}{2}\right)\Big/\left(\psi'^2-\frac{\chi'^2}{\rho}\right)-\frac{1}{\gamma-1}\rho^\gamma e^\sigma+\rho H\right]'=0 \qquad (2.18)$$

where γ is the adiabatic index, henceforth taken to be that for an ideal monatomic gas, $5/3$. Note that the divergence operator is taken in the full 3D geometry, despite the fact that the variables depend only on the 2D poloidal plane. Hence, the first term in equation (2.18), expressed in terms of partial derivatives, is

$$\underline{\nabla}\cdot\left[\left(\psi'^2-\frac{\chi'^2}{\rho}\right)\frac{\underline{\nabla}\xi}{\lambda^2}\right]=\frac{1}{\lambda}\frac{\partial}{\partial\lambda}\left[\left(\psi'^2-\frac{\chi'^2}{\rho}\right)\frac{1}{\lambda}\frac{\partial\xi}{\partial\lambda}\right]+\frac{1}{\lambda^2}\frac{\partial}{\partial z}\left[\left(\psi'^2-\frac{\chi'^2}{\rho}\right)\frac{\partial\xi}{\partial z}\right]. \qquad (2.19)$$

It is important to highlight several potential numerical challenges associated with solving equation (2.19). This PDE is of mixed type; it can be elliptic in some portions of the domain, while simultaneously hyperbolic in others. Mixed-type PDEs may lead to numerical difficulties, and care must be taken [13, 29]. While in the solar regime, the majority of the domain is in the elliptic regime, we predict that a thin hyperbolic layer appears around the location of the tachocline. We discuss this issue in Chapter 6, when such transitions become relevant.

Moreover, equation (2.18) becomes singular when $\rho\to\rho_c(\xi)\equiv\chi'^2/\psi'^2$. An application of l'Hôpital's rule implies that, in order for the second line to remain finite, then $\lambda^2\to\lambda_c^2(\xi)\equiv-\psi' L/\chi' F$. The differential operator is unable to balance this diverging

term, owing to the vanishing term inside the differential operator. Fortunately, the equations end up naturally conspiring to avoid this issue (see Chapter 6)!

2.4 Lagrangian formulation

In this section, we describe an equivalent Lagrangian description of the G–S equation, as we will use this formulation to implement our numerical methods. Such methods have been shown to be particularly suitable for solving mixed-type nonlinear PDEs with critical surfaces [83].

The similarity between equations (2.17) and (2.18) is no accident; they express the stationarity of a Lagrangian with respect to perturbations to ρ and ξ, respectively. To fit the Lagrangian on a single line, consider the following definitions:

$$\Pi_1 \equiv H + \frac{1}{2}\frac{\lambda^2 F^2}{\psi'^2} - \Phi, \tag{2.20}$$

$$\Pi_2 \equiv \frac{\gamma}{\gamma - 1} e^{\sigma}, \tag{2.21}$$

$$\Pi_3 \equiv \frac{1}{2}\left(\frac{L}{\lambda\chi'} + \frac{\lambda F}{\psi'}\right)^2. \tag{2.22}$$

The Lagrangian is then

$$\mathcal{L}\left[\xi, \rho\right] = \int_{\mathcal{D}} \left[\frac{1}{2}\left(\psi'^2 - \frac{\chi'^2}{\rho}\right)\frac{\left|\nabla\xi\right|^2}{\lambda^2} - \rho\Pi_1 + \frac{\rho^\gamma}{\gamma}\Pi_2 - \frac{\chi'^2/\rho}{\psi'^2 - \chi'^2/\rho}\rho\Pi_3\right] dV, \tag{2.23}$$

where the integral is taken over the 3D volume $\mathcal{D}$ (hence, an additional factor of λ is required when performing the area integral over the poloidal plane).

2.4.1 An important limit and a renormalization

Both the poloidal field and flow are used in the derivation of the G–S equation, and are important for deriving the flux/stream functions. However, while the magnetostatic limit is relevant to many terrestrial experiments, the outer layers of the Sun are definitively in the hydrodynamic limit [46].

For the limit of zero poloidal flow, $\chi' \to 0$, equation (2.22) appears to diverge. However, its multiplication by χ'^2 in equation (2.23) renders the Lagrangian finite, and these equations may still be used.

However, in the limit of zero poloidal field, $\psi' \to 0$, the Lagrangian (as written) indeed diverges. Hope is not lost, however; infinite Lagrangians are often still useful, as we are only interested in their stationarity [99]. In our case, there exists an appropriately renormalized version of equation (2.20) that remains finite as $\psi' \to 0$, while resulting in identical Euler–Lagrange equations:

$$H = \frac{FL}{\psi'\chi'} + \overline{H}. \tag{2.24}$$

We remark that this redefinition conversely causes the Lagrangian that uses $\overline{H}$ to diverge in the $\chi' \to 0$ limit[1].

This illustrates the usefulness of using ξ as a flux "label", as compared to using the poloidal flux ψ as the independent variable in the PDE. Moreover, consider a configuration in which the poloidal field changes sign. The standard use of ψ as the flux function would cause different surfaces to have the same label. However, if one instead uses ξ as a label of these different surfaces, there is no issue with having ψ' change sign.

[1]The treatment of $\psi' \to 0$ and $\chi' \to 0$ depends on precisely how the joint limit is taken.

Chapter 3

The Numerical Scheme

Numbers are like chickens;

if there's a hole in your code, they will find it.

—— Stuart R. Hudson

Tortoise: *Jōshū "unasked" the question.*

Achilles: *Exactly!*

—— Douglas Hofstadter, *Gödel, Escher, Bach*

3.1 Description of the numerical problem

Essentially, the goal is to solve $\delta\mathcal{L} = 0$ (equation (2.23)) for two scalar variables, ξ and ρ, within some 2D domain $\mathcal{D}$ with coordinates $\lambda \in \mathbb{R}_{\geq 0}$ and $z \in \mathbb{R}$. While the equation for ρ is an algebraic expression (2.17), the equation governing ξ is a PDE (2.18), so boundary conditions must be given for ξ. In addition, the six auxiliary scalar functions, ie, $\psi(\xi)$, $\chi(\xi)$, $F(\xi)$, $L(\xi)$, $\sigma(\xi)$, and $H(\xi)$, must be given. These are functions of ξ only, but are otherwise arbitrary. Finally, a fixed external potential Φ is given as a function of this domain. In

summary:

$$\text{solve for:} \quad \begin{cases} \xi(\lambda, z) \\ \rho(\lambda, z) \end{cases} \tag{3.1}$$

$$\text{given:} \quad \begin{cases} \text{domain:} & \mathcal{D} \subseteq \{(\lambda, z) \in \mathbb{R}^2,\ \lambda \geq 0\} \\ \text{boundary conditions:} & \alpha_{\mathrm{d}}\xi + \alpha_{\mathrm{n}}\hat{\mathbf{n}} \cdot \underline{\nabla}\xi = \beta \quad \text{on } \partial\mathcal{D} \\ \text{auxiliary functions:} & f : \xi \to \mathbb{R} \quad \forall f \in \{\psi, \chi, F, L, \sigma, H\} \\ \text{external potential:} & \Phi : (\lambda, z) \to \mathbb{R}. \end{cases} \tag{3.2}$$

3.2 Previous numerical methods

Before the author developed the numerical scheme used to produce the results of this thesis, there were several attempts that proved to be inadequate. While frustrating, there were important lessons that informed our final numerical scheme. We now briefly discuss these "learning opportunities".

3.2.1 The FLOW code

We started by using the Fortran code named FLOW developed by Guazzotto et al. [42], intended to study MHD equilibria relevant for toroidal confinement experiments. In particular, their code includes effects from both toroidal and poloidal flow, ie, it solves the generalized Grad–Shafranov equation. The case of pure toroidal rotation is not particularly difficult, as the equation is elliptic everywhere and does not contain vanishing denominators. While previous investigations generally focused on the weak poloidal flow regime, the FLOW code is particularly notable for its ability to incorporate strong poloidal flows. In particular, they were able to obtain equilibria with a discontinuous transition between a subsonic domain and a supersonic domain.

The domain is discretized into a uniform grid in (λ, z), with spatial step sizes of δ_λ and δ_z. The divergence term $\underline{\nabla} \cdot \left[\left(\psi'^2 - \frac{\chi'^2}{\rho}\right) \frac{\underline{\nabla}\xi}{\lambda^2}\right]$ in the PDE (2.18) is approximated by finite difference:

$$D[\xi,\rho]|_{i,j} = \frac{1}{\lambda_{i,j}} \left\{ \frac{1}{\delta_\lambda} \left[\left(\psi'^2_{i+1/2,j} - \frac{\chi'^2_{i+1/2,j}}{\rho_{i+1/2,j}} \right) \frac{\frac{\partial\xi}{\partial\lambda}|_{i+1/2,j}}{\lambda_{i+1/2,j}} - \left(\psi'^2_{i-1/2,j} - \frac{\chi'^2_{i-1/2,j}}{\rho_{i-1/2,j}} \right) \frac{\frac{\partial\xi}{\partial\lambda}|_{i-1/2,j}}{\lambda_{i-1/2,j}} \right] \right.$$
$$\left. + \frac{1}{\delta_z} \left[\left(\psi'^2_{i,j+1/2} - \frac{\chi'^2_{i,j+1/2}}{\rho_{i,j+1/2}} \right) \frac{\frac{\partial\xi}{\partial z}|_{i,j+1/2}}{\lambda_{i,j+1/2}} - \left(\psi'^2_{i,j-1/2} - \frac{\chi'^2_{i,j-1/2}}{\rho_{i,j-1/2}} \right) \frac{\frac{\partial\xi}{\partial z}|_{i,j-1/2}}{\lambda_{i,j-1/2}} \right] \right\}. \tag{3.3}$$

Scalar quantities on half-integer points are evaluated using values of ξ and λ equal to the average between the neighboring nodes (eg, $\chi'^2_{i+1/2,j} = \chi'^2(\xi_{i+1/2,j})$, and $\xi_{i+1/2,j} = (\xi_{i,j} + \xi_{i+1,j})/2$). Gradient quantities on half-integer points are defined as

$$\left.\frac{\partial\xi}{\partial\lambda}\right|_{i+1/2,j} = \frac{1}{\delta_\lambda}(\xi_{i+1,j} - \xi_{i,j})$$
$$\left.\frac{\partial\xi}{\partial z}\right|_{i,j+1/2} = \frac{1}{\delta_z}(\xi_{i,j+1} - \xi_{i,j}).$$

The remaining terms in the PDE (2.18) will be denoted as $A[\xi,\rho]|_{i,j}$, with derivatives given by

$$\left.\frac{\partial\xi}{\partial\lambda}\right|_{i,j} = \frac{1}{2\delta_\lambda}(\xi_{i+1,j} - \xi_{i-1,j})$$
$$\left.\frac{\partial\xi}{\partial z}\right|_{i,j} = \frac{1}{2\delta_z}(\xi_{i,j+1} - \xi_{i,j-1}).$$

The code then solves the finite difference equation

$$D[\xi,\rho]|_{i,j} + A[\xi,\rho]|_{i,j} = 0 \quad \forall i,j$$

by updating $\xi_{i,j}$ as follows:

$$\xi_{i,j}^{n+1} \to \xi_{i,j}^{n} - \left(\frac{\partial D[\xi,\rho]|_{i,j}}{\partial \xi_{i,j}} \right)^{-1} \left(D[\xi,\rho]|_{i,j} + A[\xi,\rho]|_{i,j} \right).$$

This is essentially a Newton's method, except it only uses the derivative associated with the divergence term D, neglecting the derivative associated with the algebraic term A. For magnetic confinement experiments, such an approximation is generally valid (as $\partial A/\partial \xi$ tends to be subdominant compared to the terms associated with D). However, in the solar regime, the poloidal terms are small compared to the toroidal terms, and the change in A with respect to ξ can be significant. We found that the code does not converge unless this change is incorporated, ie,

$$\xi_{i,j}^{n+1} \to \xi_{i,j}^{n} - \left(\frac{\partial D[\xi,\rho]|_{i,j}}{\partial \xi_{i,j}} + \frac{\partial A[\xi,\rho]|_{i,j}}{\partial \xi_{i,j}} \right)^{-1} \left(D[\xi,\rho]|_{i,j} + A[\xi,\rho]|_{i,j} \right).$$

Moreover, we implemented several additional modifications to the code relevant for running in the solar regime. For example, we allowed for the grid to be specified in spherical coordinates (r, θ), including the appropriate changes to the divergence operator. We also allowed for variable grid spacing (allowing for, eg, more radial resolution at the surface), again appropriately modifying the terms in the divergence operator.

To determine the density, the FLOW code uses a root solver to find all the possible solutions to the Bernoulli equation (2.17), and a method for choosing the appropriate root is required. While there is an option for transonic equilibria, the method assumes that there is a discontinuous switch from the subsonic to the supersonic root. Moreover, this choice of sub/supersonic root is selected using a single cutoff value for ξ (determined at each iteration) intended to separate the two domains, thus constraining the transition to align with the flux/stream surfaces. However, the trans-Alfvénic case we are considering is

notably different: the surfaces separating the different choices of solutions for the density are not aligned with the flux/stream surfaces, and incorporating an appropriate method for determining which solution for ρ to choose at each gridpoint appears highly nontrivial.

3.2.2 Our old finite element method

Given the difficulties associated with adapting the FLOW code, we developed our own solver of the same set of equations. The major changes included in this attempt were:

1. A flexible domain, taking the form of an unstructured triangular mesh.
2. An adaptive triangular mesh, shifting nearby vertices to exactly coincide with the Alfvén surface at each iteration.
3. Piecewise continuous polynomials are used as the basis functions.
4. Gaussian quadrature to evaluate the integrals is used to solve the weak form of the PDE.
5. Either a root finder or the weak form is used to solve the Bernoulli equation.

Solving the weak form of the PDE

The weak formulation allows for a discontinuous $\nabla\xi$, as compared to the original PDE. Such a discontinuous gradient could result in the original PDE being not well-defined. To obtain the weak form of the PDE, multiply it by a test function $g(\underline{\mathbf{x}})$ and integrate the differential

operator by parts:

$$\int_{\mathcal{D}} \left\{ g(\underline{\mathbf{x}}) \underline{\nabla} \cdot \left[\left(\psi'^2 - \frac{\chi'^2}{\rho} \right) \frac{\underline{\nabla}\xi}{\lambda^2} \right] - g(\underline{\mathbf{x}}) \left(\psi'^2 - \frac{\chi'^2}{\rho} \right)' \frac{|\underline{\nabla}\xi|^2}{\lambda^2} \right\} dV + \int_{\mathcal{D}} g(\underline{\mathbf{x}}) A(\underline{\mathbf{x}}, \xi, \rho)\, dV = 0$$

$$\begin{aligned} \implies & \int_{\partial\mathcal{D}} \left[g(\underline{\mathbf{x}}) \left(\psi'^2 - \frac{\chi'^2}{\rho} \right) \right] \frac{\hat{\mathbf{n}} \cdot \underline{\nabla}\xi}{\lambda^2} dS \\ & - \int_{\mathcal{D}} \left[\left(\psi'^2 - \frac{\chi'^2}{\rho} \right) \frac{\underline{\nabla} g \cdot \underline{\nabla}\xi}{\lambda^2} + g(\underline{\mathbf{x}}) \left(\psi'^2 - \frac{\chi'^2}{\rho} \right)' \frac{|\underline{\nabla}\xi|^2}{\lambda^2} \right] dV \\ & + \int_{\mathcal{D}} g(\underline{\mathbf{x}}) A(\underline{\mathbf{x}}, \xi, \rho)\, dV = 0. \end{aligned} \tag{3.4}$$

If a function $\xi(\underline{\mathbf{x}})$ satisfies this relation for all test functions $g(\underline{\mathbf{x}})$, then it is said to be a weak solution of the PDE. We remark that the function A used here does not contain the term involving $|\underline{\nabla}\xi|^2$, as it did in the FLOW code.

The weak form of the Bernoulli equation is comparatively simpler:

$$\begin{aligned} \int_{\mathcal{D}} g(\underline{\mathbf{x}}) \Bigg\{ & \frac{1}{2} \frac{\chi'^2}{\rho^2} \frac{|\underline{\nabla}\xi|^2}{\lambda^2} + \frac{1}{2} \frac{\chi'^2}{\rho^2} \left[\left(\frac{L}{\lambda} + \frac{\lambda \chi' F}{\psi'} \right) \Big/ \left(\psi'^2 - \frac{\chi'^2}{\rho} \right) \right]^2 \\ & - \frac{1}{2} \frac{\lambda^2 F^2}{\psi'^2} + \frac{\gamma}{\gamma - 1} \rho^{\gamma - 1} e^{\sigma} + \Phi - H(\xi) \Bigg\} dV = 0 \end{aligned} \tag{3.5}$$

The unstructured, adaptive discretization

The domain is discretized into an unstructured triangular mesh using the code GMSH [33]. The discretized function space for both g and ξ are the continuous, piecewise cubic functions over these triangles. The cubic polynomial on each triangle has 10 degrees of freedom; hence 10 nodes are associated to each triangle (1 on each of the corners, 2 equally spaced along each edge, and 1 at the barycenter). The basis function g_i associated to node i is the continuous, piecewise cubic with the value 1 at node i and 0 for all others. Discretizing $\xi\,(\underline{\mathbf{x}})$

as $\sum \xi_j g_j$, equation (3.4) becomes a matrix equation $M_{ij}\xi_j + b_i = 0$ for the coefficients ξ_j:

$$\begin{aligned}
&\int_{\partial\mathcal{D}} \left[g \left(\psi'^2 - \frac{\chi'^2}{\rho} \right) \right] \frac{\hat{\mathbf{n}} \cdot \underline{\nabla} \xi}{\lambda^2} dS \\
&\underbrace{- \int_{\mathcal{D}} \left[\left(\psi'^2 - \frac{\chi'^2}{\rho} \right) \frac{\underline{\nabla} g_i}{\lambda^2} + \left(\psi'^2 - \frac{\chi'^2}{\rho} \right)' \frac{g_i}{\lambda^2} \underline{\nabla} \xi \right] \cdot \underline{\nabla} g_j \, \xi_j dV}_{M_{ij}\xi_j} \\
&\underbrace{+ \int_{\mathcal{D}} g_i A(\underline{\mathbf{x}}, \xi, \rho) \, dV}_{b_i} = 0 \qquad \forall i.
\end{aligned} \tag{3.6}$$

To approximate the integrals, we use Gaussian quadrature. Since we are multiplying pairs of basis functions of order 3, we require accuracy for polynomials up to order 6. This requires 12 evaluation points for the triangles and 4 evaluation points for the lines (edges). Thus, the equations we are solving are:

$$\begin{aligned}
&\sum_{n=1}^{N_l} \left[\sum_{q=1}^{4} w_{qn} g_i \left(\psi'^2 - \frac{\chi'^2}{\rho} \right) \xi_j \hat{\mathbf{n}} \cdot \underline{\nabla} g_j \right] \\
&- \sum_{n=1}^{N_t} \left\{ \sum_{q=1}^{12} w_{qn} \xi_j \left[\left(\psi'^2 - \frac{\chi'^2}{\rho} \right) \frac{\underline{\nabla} g_i}{\lambda^2} + \left(\psi'^2 - \frac{\chi'^2}{\rho} \right)' \frac{g_i}{\lambda^2} \underline{\nabla} \xi \right] \cdot \underline{\nabla} g_j \right. \\
&\qquad \left. + \sum_{q=1}^{12} w_{qn} g_i A(\underline{\mathbf{x}}, \xi, \rho) \right\} = 0
\end{aligned} \tag{3.7}$$

$$\begin{aligned}
&\sum_{n=1}^{N_t} \left\{ \sum_{q=1}^{12} w_{qn} g_i \left[\frac{1}{2} \frac{\chi'^2}{\rho^2} \frac{|\underline{\nabla} \xi|^2}{\lambda^2} + \frac{1}{2} \frac{\chi'^2}{\rho^2} \left(\left(\frac{L}{\lambda} + \frac{\lambda \chi' F}{\psi'} \right) \Big/ \left(\psi'^2 - \frac{\chi'^2}{\rho} \right) \right)^2 \right. \right. \\
&\qquad \left. \left. - \frac{1}{2} \frac{\lambda^2 F^2}{\psi'^2} + \frac{\gamma}{\gamma - 1} \rho^{\gamma - 1} e^{\sigma} + \Phi - H(\xi) \right] \right\} = 0,
\end{aligned} \tag{3.8}$$

where N_l and N_t are the numbers of lines and triangles in the grid respectively, and the parts inside the sums are evaluated at $\underline{\mathbf{x}}_{qn}$ (the q^{th} quadrature point of element n) with associated weight w_{qn}.

As the domain is unstructured, it is possible to specify an arbitrary boundary. Moreover, one can specify variable minimum resolutions for different portions of the domain. This provides additional flexibility, allowing for simultaneous simulation of the global structure as well as smaller details (eg, the NSSL).

If one evaluates terms in the PDE or Bernoulli equation too close to the Alfvén surface, then one is required to evaluate the ratio of two small numbers, a familiar source of numerical hot water. To remedy this issue, we found that it was advantageous to have triangles completely within the super-Alfvénic or sub-Alfvénic regimes, with the edges of the triangles being aligned with the Alfvén surface. As the PDE and Bernoulli equation are only evaluated using the quadrature points, which are completely interior to the triangles, this protocol essentially solved the aforementioned issue of small denominators.

While constructing such a versatile numerical scheme was an important learning exercise, the many moving parts associated with our unstructured, adaptive discretization proved to add unnecessary complications to the already subtle problem of crossing the Alfvén surface. As such, we constructed a new (simpler and more elegant) numerical scheme that crosses the Alfvénic border with less baggage.

3.3 New numerical scheme

In this section, we discuss our final, more elegant numerical scheme for solving $\delta\mathcal{L} = 0$ (equation (2.23)).

3.3.1 Discretizing the Lagrangian

Our numerical scheme begins by discretizing the Lagrangian, as opposed to discretizing the resulting Euler–Lagrange equations.

The spherical domain is discretized in (r, θ) space as an $N_r \times N_\theta$ regular square mesh. The function ξ is represented as piecewise linear[1] over the squares by values on the integer vertices (i, j). The function ρ is represented as piecewise constant quantities; the average density in a square is given by values on the centered half-integer points $(i + 1/2, j + 1/2)$. Let us denote these vectors as ξ_d and ρ_d, the discrete version of Lagrangian (2.23) is then:

$$\mathcal{L}_d\left[\xi_d, \rho_d\right] = \sum_{i=1}^{N_r}\sum_{j=1}^{N_\theta}\left\{\left[\frac{1}{2}\left(\psi'^2 - \frac{\chi'^2}{\rho}\right)\frac{\left|\underline{\nabla}\xi\right|^2}{\lambda^2} - \rho\Pi_1 + \frac{\rho^\gamma}{\gamma}\Pi_2 - \frac{\chi'^2/\rho}{\psi'^2 - \chi'^2/\rho}\rho\Pi_3\right]\lambda r\right\}_{i+1/2,j+1/2}. \tag{3.9}$$

We express ξ and $\left|\underline{\nabla}\xi\right|^2$on the half-integer points as follows:

$$\xi_{i+1/2,j+1/2} = \frac{1}{4}\left(\xi_{i,j} + \xi_{i+1,j} + \xi_{i,j+1} + \xi_{i+1,j+1}\right) \tag{3.10}$$

$$\begin{aligned}\left|\underline{\nabla}\xi\right|^2_{i+1/2,j+1/2} = {} & \frac{1}{2}\left[\left(\frac{\xi_{i+1,j} - \xi_{i,j}}{\Delta_r}\right)^2 + \left(\frac{\xi_{i+1,j+1} - \xi_{i,j+1}}{\Delta_r}\right)^2\right] \\ & + \frac{1}{2}\left[\left(\frac{\xi_{i,j+1} - \xi_{i,j}}{r_i\Delta_\theta}\right)^2 + \left(\frac{\xi_{i+1,j+1} - \xi_{i+1,j}}{r_{i+1}\Delta_\theta}\right)^2\right].\end{aligned} \tag{3.11}$$

3.3.2 Boundary conditions

When either the pole and equator are a part of the boundary of the simulation domain, their rotational and reflectional symmetries motivate a natural choice of boundary condition, viz, Dirichlet boundary conditions on the axis and "Neumann-like" boundary conditions on the equator. However, other choices might be relevant for the inner and outer boundary conditions. We now discuss the case of boundary conditions imposed by these symmetries, and address the case of other choices in the next section.

[1]The functions over the squares are linear in each direction individually ($c + c_r r + c_\theta\theta + c_{r\theta}r\theta$).

For the sake of explanation, let us represent the continuous Lagrangian as

$$\mathcal{L}[\xi, \rho] = \int_{\mathcal{D}} \left[f \left| \underline{\nabla} \xi \right|^2 - g \right] dV, \tag{3.12}$$

where

$$\begin{aligned} f &= \psi'^2 - \frac{\chi'^2}{\rho}, \\ g &= \rho \Pi_1 - \frac{\rho^\gamma}{\gamma} \Pi_2 + \frac{\chi'^2/\rho}{\psi'^2 - \chi'^2/\rho} \rho \Pi_3. \end{aligned}$$

Taking the variation with respect to ξ and integrating by parts yields

$$\delta \mathcal{L} = \int_{\partial \mathcal{D}} f(\hat{n} \cdot \underline{\nabla} \xi) \delta \xi dS - \int_{\mathcal{D}} \left[\underline{\nabla} \cdot (f \underline{\nabla} \xi) - \frac{\partial f}{\partial \xi} \left| \underline{\nabla} \xi \right|^2 + \frac{\partial g}{\partial \xi} \right] \delta \xi dV. \tag{3.13}$$

For both Dirichlet and Neumann boundary conditions, the integral over the boundary vanishes. Thus, setting this variation to zero for all $\delta \xi$ (that respect the boundary conditions) implies that the integral over the volume must be identically zero, which in turn implies the PDE (equation (2.18)).

3.3.3 Unconstraining the boundary conditions

Our domain is often completely within the interior of the Sun and there is no natural choice of boundary conditions. In these cases, we desire solutions that satisfy the G–S equations in the interior of the domain, while allowing the "boundary conditions" to vary such that the solution has some other desired properties. In particular, we desire smooth solutions, such that the short wavelength oscillations (see Section 5.2 in Chapter 4) are suppressed. This turned out to be highly nontrivial, and we tried several approaches before converging on a solution.

First, we attempted to iteratively solve the PDE (2.18) and Bernoulli equation (2.17) using Dirichlet boundary conditions. For example, one could initialize $\underline{\mathbf{x}}$ with a vector satisfying these boundary conditions, and updating it using

$$\underline{\mathbf{x}}^{n+1} - \underline{\mathbf{x}}^{n} = -\left[\begin{array}{c|c} \underline{\nabla}_a \underline{\nabla}_a \mathcal{L} & 0 \\ \hline 0 & \underline{\underline{\mathbf{I}}} \end{array}\right]^{-1} \left[\begin{array}{c} \underline{\nabla}_a \mathcal{L} \\ \hline 0 \end{array}\right], \tag{3.14}$$

where we have the collected the degrees of freedom ξ_d and ρ_d into a single vector $\underline{\mathbf{x}} = (\underline{\mathbf{x}}_a, \underline{\mathbf{x}}_b)$, where $\underline{\mathbf{x}}_b$ are the values associated to ξ at the boundary points, and $\underline{\mathbf{x}}_a$ is everything else.

While in principle, one could compute how the solution changes as one varies the values of the boundary conditions, searching for a resulting global solution without the short wavelength oscillations turned out to be difficult and inefficient.

Another method we tried was to take the surface integral into account (equation (3.13)), and instead solve for

$$\delta\mathcal{L} - \mathcal{B} \cdot \delta\xi = 0,$$
$$\mathcal{B} = f(\hat{n} \cdot \underline{\nabla}\xi) \quad \text{on } \partial\mathcal{D}.$$

In the discretized version, we evaluate quantities at the half-integer boundary point by Taylor expansion. Note that, while the boundary term $\mathcal{B}$ itself depends on the interior grid points, the expression for $\delta\xi$ evaluated on the boundary depends only on the boundary points.

We are now essentially solving the system

$$\underline{\nabla}\mathcal{L} - \underline{\mathcal{B}} = 0, \tag{3.15}$$

where we have dropped the subscript d, as clearly the numerical method acts on discrete quantities. Equation (3.15) can be visualized as the following matrix equation:

$$\text{find} \quad \underline{\mathbf{x}} = \left[\begin{array}{c} \underline{\mathbf{x}}_a \\ \hline \underline{\mathbf{x}}_b \end{array}\right] \quad \text{such that} \quad \left[\begin{array}{c} \underline{\nabla}_a \mathcal{L} \\ \hline \underline{\nabla}_b \mathcal{L} - \underline{\mathcal{B}}_b \end{array}\right] \left[\begin{array}{c} \underline{\mathbf{x}}_a \\ \hline \underline{\mathbf{x}}_b \end{array}\right] = 0 \tag{3.16}$$

To solve this system, we employ Newton's method. We start with an initial guess $\underline{\mathbf{x}}^0$ and update it as follows:

$$\underline{\mathbf{x}}^{n+1} - \underline{\mathbf{x}}^n = - \left[\begin{array}{c|c} \underline{\nabla}_a \underline{\nabla}_a \mathcal{L} & \underline{\nabla}_b \underline{\nabla}_a \mathcal{L} \\ \hline \underline{\nabla}_a \underline{\nabla}_b \mathcal{L} - \underline{\nabla}_a \underline{\mathcal{B}}_b & \underline{\nabla}_b \underline{\nabla}_b \mathcal{L} - \underline{\nabla}_b \underline{\mathcal{B}}_b \end{array}\right]^{-1} \left[\begin{array}{c} \underline{\nabla}_a \mathcal{L} \\ \hline \underline{\nabla}_b \mathcal{L} - \underline{\mathcal{B}}_b \end{array}\right]. \tag{3.17}$$

This is essentially an attempt to discretize and solve a formally underdetermined system, and therefore should have as many solutions as there are potential boundary conditions. The space of possible Dirichlet boundary conditions is a $|b|$-dimensional space, where $|b|$ is the number of grid points on the boundary. This freedom in the solution for $\underline{\mathbf{x}}$, in theory, should correspond to a $|b|$-dimensional null space of the matrix of second derivatives. While this matrix might not be exactly singular (as it is a discretized approximation of equation (3.15)), simply inverting it as in equation (3.17) frequently inhibits convergence (as it is indeed ill-conditioned).

An apparently straightforward solution to this problem would be to consider a pseudoinverse with a cutoff for the eigenvalues that renders these unconstrained directions as part of the null space. However, choosing an appropriate cutoff proved to be tricky, as the

eigenvalues associated with these unconstrained directions are not well-separated from the rest of the spectrum.

Instead, our final approach aims to simultaneously:

1. Converge towards a solution for $\underline{\nabla}_a \mathcal{L}(\underline{\mathbf{x}}) = \underline{\mathbf{0}}$,
2. Allow the boundary values to vary freely, and
3. Iteratively "nudge" the obtained solution towards one that is smooth, ie, without the undesired short wavelength oscillations.

3.3.4 Obtaining smooth solutions

To this end, we construct the matrix equation that allows for the entire $\underline{\mathbf{x}}$ to vary, while only attempting to satisfy the equations $\underline{\nabla}_a \mathcal{L}(\underline{\mathbf{x}}) = \underline{\mathbf{0}}$, ie,

$$\underline{\mathbf{x}}^{n+1} - \underline{\mathbf{x}}^{n} = - \left[\begin{array}{c|c} \underline{\nabla}_a \underline{\nabla}_a \mathcal{L} & \underline{\nabla}_b \underline{\nabla}_a \mathcal{L} \\ \hline 0 & 0 \end{array}\right]^{\dagger} \left[\begin{array}{c} \underline{\nabla}_a \mathcal{L} \\ \hline 0 \end{array}\right], \tag{3.18}$$

where now the pseudoinverse must be taken, as the matrix is explicitly not full rank.

To move the solution towards one with our desired properties, we must characterize the directions associated with the extra degrees of freedom, namely those such that $\underline{\nabla}_a \mathcal{L}(\underline{\mathbf{x}} + \delta\underline{\mathbf{x}}) = \mathcal{O}(|\delta\underline{\mathbf{x}}|^2)$. To this end, we perform a singular value decomposition of this matrix, ie, $(\underline{\nabla}\underline{\nabla}\mathcal{L}) = \underline{\underline{\mathbf{U}}}\,\underline{\underline{\mathbf{\Sigma}}}\,\underline{\underline{\mathbf{V}}}$, where $\underline{\underline{\mathbf{U}}}$ and $\underline{\underline{\mathbf{V}}}$ are unitary square matrices, and $\underline{\underline{\mathbf{\Sigma}}}$ is the diagonal matrix of singular values. The rows of $\underline{\underline{\mathbf{V}}}$ form an orthonormal basis for $\underline{\mathbf{x}}$, and the bottom rows, $\underline{\underline{\mathbf{V}}}_b$, correspond precisely to the linearized null space, ie, the directions we

want for $\delta\underline{\mathbf{x}}$:

$$\left[\begin{array}{c|c} \underline{\nabla}_a\underline{\nabla}_a\mathcal{L} & \underline{\nabla}_b\underline{\nabla}_a\mathcal{L} \\ \hline 0 & 0 \end{array}\right] = \left[\begin{array}{c|c} \underline{\underline{\mathbf{U}}}_a & 0 \\ \hline 0 & 0 \end{array}\right] \left[\begin{array}{c|c} \underline{\underline{\mathbf{\Sigma}}}_a & 0 \\ \hline 0 & 0 \end{array}\right] \left[\begin{array}{c} \underline{\underline{\mathbf{V}}}_a \\ \hline \underline{\underline{\mathbf{V}}}_b \end{array}\right]. \tag{3.19}$$

We can drop the unnecessary zero entries, ie

$$\left[\begin{array}{c|c} \underline{\nabla}_a\underline{\nabla}_a\mathcal{L} & \underline{\nabla}_b\underline{\nabla}_a\mathcal{L} \end{array}\right] = \left[\begin{array}{c} \underline{\underline{\mathbf{U}}}_a \end{array}\right] \left[\begin{array}{c|c} \underline{\underline{\mathbf{\Sigma}}}_a & 0 \end{array}\right] \left[\begin{array}{c} \underline{\underline{\mathbf{V}}}_a \\ \hline \underline{\underline{\mathbf{V}}}_b \end{array}\right]. \tag{3.20}$$

The pseudoinverse can now be expressed as:

$$\left[\begin{array}{c|c} \underline{\nabla}_a\underline{\nabla}_a\mathcal{L} & \underline{\nabla}_b\underline{\nabla}_a\mathcal{L} \end{array}\right]^\dagger = \left[\begin{array}{c|c} \underline{\underline{\mathbf{V}}}_a^\top & \underline{\underline{\mathbf{V}}}_b^\top \end{array}\right] \left[\begin{array}{c} \underline{\underline{\mathbf{\Sigma}}}_a^{-1} \\ \hline 0 \end{array}\right] \left[\begin{array}{c} \underline{\underline{\mathbf{U}}}_a^\top \end{array}\right]. \tag{3.21}$$

In particular, each iteration of the numerical scheme consists of two steps:

1. A step that reduces the error in the solution, and

2. A step that reduces the oscillatory nature of the solution.

The first step simply uses the pseudoinverse of the (now rectangular) matrix of sec-

ond derivatives of $\mathcal{L}$ to perform a Newton step:

$$\underline{\mathbf{x}}^{n+1} - \underline{\mathbf{x}}^{n} = -\left[\begin{array}{c|c} \underline{\nabla}_a \underline{\nabla}_a \mathcal{L} & \underline{\nabla}_b \underline{\nabla}_a \mathcal{L} \end{array}\right]^{\dagger} \left[\begin{array}{c} \underline{\nabla}_a \mathcal{L} \end{array}\right]. \tag{3.22}$$

In general, this update reduces the error of the solution. However, in the solar regime, short-wavelength oscillations can appear, which we fix in the second step.

The second step adds to the solution a linear combination of the rows of $\underline{\underline{\mathbf{V}}}$ associated with the boundary:

$$\underline{\mathbf{x}}^{n+1} \to \underline{\mathbf{x}}^{n+1} + \underline{\mathbf{c}}^{\top} \underline{\underline{\mathbf{V}}}_b. \tag{3.23}$$

The precise values of the coefficients $\underline{\mathbf{c}}$ are chosen to minimize a cost function that quantifies the amount of short-wavelength oscillations, which we choose to be

$$\mathcal{S}[\xi] = \int_{\mathcal{D}} \left(\nabla^2 \xi\right)^2 dV. \tag{3.24}$$

Our motivation for choosing this cost function is twofold. First, it provides an intuitive measure of smoothness, strongly penalizing higher frequencies. Second, it is numerically convenient as it can be minimized exactly (since it is a quadratic function of $\underline{\mathbf{c}}$).

We solve this minimization problem by first constructing a discrete version of the ∇^2 operator, a matrix $\underline{\underline{\mathbf{N}}}$ such that $\underline{\underline{\mathbf{N}}}\underline{\mathbf{x}}$ is a vector of the finite-difference approximations to $\nabla^2 \xi$ at each grid point. Then the coefficients $\underline{\mathbf{c}}$ (equation (3.23)) that minimize $\mathcal{S}[\xi]$ (equation (3.24)) are given by

$$\underline{\mathbf{c}} = -\left(\underline{\underline{\mathbf{V}}}_b \underline{\underline{\mathbf{N}}}^{\top} \underline{\underline{\mathbf{N}}} \underline{\underline{\mathbf{V}}}_b^{\top}\right)^{-1} \left(\underline{\underline{\mathbf{V}}}_b \underline{\underline{\mathbf{N}}}^{\top} \underline{\underline{\mathbf{N}}} \underline{\mathbf{x}}^{n+1}\right). \tag{3.25}$$

While the smoothed solution $\underline{\mathbf{x}}^{n+1}$ in general does not satisfy $\nabla_a \mathcal{L} = 0$, repeating these two steps iteratively converges on a smooth solution that does (to within some desired level of accuracy).

3.3.5 Validation of the numerical methods

Figure 3.1 shows a numerical validation of our method, demonstrating that it converges to the correct solution with the appropriate scaling.

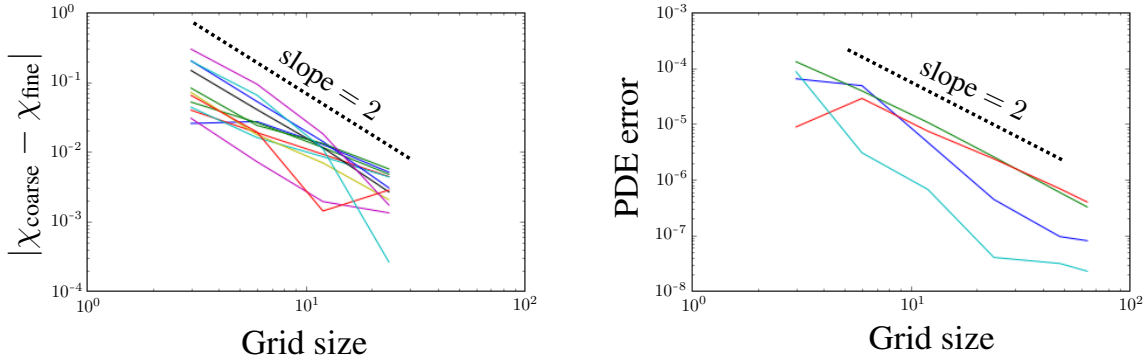

Figure 3.1: **Validation of numerical method.** Curves represent error in the PDE at several fixed representative points in the interior. These figures demonstrate that error decreases quadratically as a function of resolution, as desired. *Left*: **Grid convergence.** We consider the value of ξ at 12 fixed points in a global equilibrium simulation as a function of the grid resolution, using Dirichlet boundary conditions at the axis, reflecting boundary conditions at the equator, and Neumann boundary conditions for the top and bottom. We consider 4×4, 7×7, 13×13, 25×25, and compared them to the values obtained for a 49×49 grid. *Right*: **Solution consistency.** To verify that the solutions are indeed solving the correct equation, we measure the error in equation (2.18) using an alternative method. Namely, we employ a finite-difference approximation to the differential operator.

Our numerical method will now serve as director of the third and final trilogy in this thesis: the Convection Zone (Chapter 4), the Near Surface Shear Layer (Chapter 5), and the Tachocline (Chapter 6).

Chapter 4

The Convection Zone

Something so complicated, like a cloud,
so unstable, so varying,
should have a simple rule behind it.

—— Benoit Mandelbrot

In this chapter, we describe how the G–S formalism can be used to model the solar convection zone (CZ). We start with an overview of basic observational characteristics of the CZ, and review models that attempt to explain these features (Section 4.1). We then describe a simplified analytic model by S.A. Balbus, which is based on the principle of thermal wind balance (Section 4.2). We then show how our principled approach suggests a slight modification to the Balbus Ansatz, and produces similar agreement with observations (Sections 4.4, 4.5, and 4.6).

4.1 Characteristics of the convection zone

4.1.1 Basic properties

Radiative diffusion is an efficient mechanism of energy transport in the hot, dense core of the Sun. As a result, the entropy increases as a function of radius, and this radiative interior is convectively stable. However, as the temperature decreases with radius, the efficiency of radiative diffusion also decreases, and the entropy gradient reverses, seeding the convective instability as per the Schwarzschild criterion [82]. The efficient mixing of fluid elements causes the entropy profile to be essentially flat in this convection zone, with only a small superadiabatic profile in dynamic equilibrium with convective energy transport. Basic 1D models of radial energy transport throughout the solar interior predict an outer convective layer for stars with $\sim 0.5 - 1.5$ solar masses [50]. While the approximate location of the base of the convection zone can be estimated via such models, it was not until spherical helioseismology (see Section 1.4.1) that its depth was accurately measured to be $\sim 70\%$ of the solar radius.

These 1D models of radial energy transport treat convection as a transport process that is essentially instantaneous compared to the global timescale of energy transport. Hence, they do not offer predictions about the characteristics of this convection. However, a loose understanding of the scaling of the convective velocities can be obtained via *mixing length theory* (MLT) [62]. MLT assumes a marginally superadiabatic background profile in hydrostatic equilibrium. An element of fluid at height z that is slightly displaced is assumed to rise some fraction α of the pressure scale height $H_p = -dz/d\ln p(z)$ before dissipating its energy content. Equating the kinetic energy of this element to the work done on it by the buoyancy force gives a characteristic speed, and therefore an approximate convective flux F_c. The resulting scaling of the velocity is given by $v_r \sim \mathcal{O}((F_c/\rho)^{1/3})$.

However, observations from local helioseismology suggest that MLT overestimates these velocities, especially in the deeper portions of the CZ [49] (see Table 4.1.1). Moreover, simulations of the full CZ generally exhibit substantially higher convective velocities at large scales [49]. This discrepancy between the observations and models is commonly known in the literature as the "convective conundrum" [67]. Indeed, these global simulations should be taken with a grain of salt as they usually cannot operate in the correct regime. Not only is the correct Reynolds number orders of magnitude smaller than is currently accessible, but they also often use a modified luminosity and rotation rate to obtain solar-like profiles [65].

Quantity	Base	Surface
Radius	$5 \cdot 10^8$ m	$7 \cdot 10^8$ m
Mass density	200 kg m^{-3}	1.0 kg m^{-3}
Sound speed	$2.3 \cdot 10^5$ m s^{-1}	$8.0 \cdot 10^4$ m s^{-1}
Toroidal field	$\lesssim 300$ kG	≤ 60 kG
Poloidal field	~ 10 G (?)	~ 10 G
Toroidal flow	$\lesssim 1300$ m s^{-1}	$\lesssim 2000$ m s^{-1}
Poloidal flow	$\lesssim 1$ m s^{-1} (?)	$\sim 10 - 20$ m s^{-1}
Convective velocities	~ 10 m s^{-1} (?)	~ 1000 m s^{-1} (?)
Plasma beta	$\gtrsim 10^5$	$\gtrsim 10^3$
Toroidal Alfvénic Mach number	$\sim \mathcal{O}(1)$	$\gtrsim \mathcal{O}(10)$
Poloidal Alfvénic Mach number	$\sim \mathcal{O}(1)$ (?)	$\sim \mathcal{O}(10^2)$ (?)
Rossby number	$< \mathcal{O}(1)$	$\gtrsim \mathcal{O}(1)$

4.1.2 Differential rotation: fast equator, slow poles

Gastine et al. [32] showed that rotating stratified flows generally operate in two broad regimes: fast rotators have Coriolis forces that dominate over buoyancy, while slow rotators have the opposite. Fast rotators generally have a prograde equatorial flow, while slow

rotators have a retrograde equatorial flow. As the solar equator rotates faster than its poles, the Sun is likely operating in the fast-rotator regime. However, it is somewhat special in the sense that it is rather close to this transition. Moreover, as the Sun is continually slowing its rotation via magnetic breaking, there is even the possibility of it being in hysteresis between these two flow regimes.

The mechanism for equatorial acceleration is generally thought to be due to hydrodynamic properties, namely the Reynolds stresses associated with Coriolis forces acting upon convective motions (see [16] for a physically intuitive overview). Essentially, rotationally-constrained convection tends to produce rotating columns of fluid aligned with the axis. Inward displacements of these columns in a conical shell cause the column to lengthen and therefore become narrower, giving them an additional prograde rotation via conservation of angular momentum. Conversely, outward displacements have the opposite effect. The effect of these changes to rotation on neighboring columns serves to propagate these perturbations in the prograde direction, an effect known as Rossby waves. When the boundary is spherical, these Rossby waves propagate faster further from the axis, seeding the initial prograde equatorial flow. This is further reinforced by the mean flow instability, wherein the flow shears the convective structures, leading to Reynolds stresses that transport angular momentum outward. In slow rotators, the mechanism of differential rotation is relatively simpler: the strong convection effectively mixes angular momentum, yielding faster rotation near the axis.

4.1.3 Differential rotation: tilted isorotation contours

In the bulk of the CZ (ie, away from its boundaries), the isorotation contours are tilted radially. This deviation from the cylindrical rotation of Taylor–Proudman balance requires a source of azimuthal vorticity, and the commonly posited source is baroclinic forcing,

as it requires the poles to be only ~ 10 K warmer than the equator to match observations. Although this gradient cannot be directly measured, some simulations have managed to obtain solar-like tilted contours through this effect, such as the 2D mean-field hydrodynamic models of Kitchatinov & Rüdiger [59] and Rempel [78]. The 3D simulations of Miesch [66] also found a similar tilting of contours, albeit with an imposed entropy gradient at the base of the CZ. However, most 3D simulations have found rotation profiles closer to the Taylor–Proudman state than observations [27].

4.1.4 Meridional circulation

The meridional (poloidal) flow is relatively less constrained by observations; the only consensus seems to be that there is a ~ 20 m s^{-1} poleward flow at mid-latitudes at the surface [77]. As the meridional flow is not thought to penetrate the radiative interior [35], this observation is often extrapolated to suggest a single recirculating cell in each of the north and south hemispheres, with an equatorward return flow near the base of the CZ. Mean-field models of the solar cycle (eg, Babcock—Leighton) frequently use such a profile [24]. However, in Zhao et al. [107], local helioseismological measurements were found to implicate an equatorward return flow closer to the surface, indicating a more complex topology than previously assumed. The large-scale magnetohydrodynamic (MHD) simulations in Passos et al. [73, 74, 75] corroborated this picture, suggesting a multicelled pattern with strong axial alignment near the equator.

4.2 Thermal wind balance and the Balbus model

In an attempt to find simple closed form solutions for the CZ rotation, Balbus [6] found strikingly good agreement with observations using a very simple model. Its two ingredients are: differential rotation in thermal wind balance (TWB; ie, baroclinic forcing in the hydrostatic

limit), and the assumption that the aspherical part of the entropy is constant along isorotation contours. Indeed, when differential rotation is observed in solar simulations, it appears to be in dominant balance with a latitudinal entropy gradient throughout the bulk of the CZ [75]. The second assumption, however, is more questionable, although possible mechanisms for this alignment were posited by Balbus et al. [7, 8, 9, 10], including a marginally stable magnetobaroclinic mode, and a dynamic alignment of convective structures due to rotational shear.

4.3 The Grad–Shafranov formalism as a principled simplified model

Our framework is motivated by the observation that a similar alignment of contours naturally appears in the solution to axisymmetric ideal MHD equilibrium with flows. The equation governing this system, generalizing the standard Grad–Shafranov (G–S) approach for static plasmas, was derived by several authors (eg, Hameiri [48], Lovelace et al. [63], and Goedbloed & Lifschitz [37]). In this framework, certain quantities are flux/stream functions, ie, they are constant along the surfaces traced out by the poloidal field and flow.

For the assumed closure of adiabatic flows, entropy is one such stream function. In the limit where the poloidal field is strong compared to poloidal flow, toroidal rotation is also a stream function. This would *seem* to imply Balbus's assumption of aligned entropy and isorotation contours. However, observations of the mean field and flow at the solar surface suggest that the CZ is in the opposite limit, where the poloidal flow dominates over the poloidal field. In this limit, angular momentum replaces rotation as a stream function, implying that the natural equilibrium prescription is for entropy to align instead with angular momentum. This case was also considered by Balbus in [6], but was discarded, as their

initial results did not qualitatively match helioseismic observations. However, here we demonstrate that the freedom in choosing the form of the stream functions in the generalized G–S framework allows the theoretical model to match more closely with observations.

4.4 Comparison with Balbus model

The first assumption in Balbus' model [6] is that of TWB. It considers a rotating fluid with a background state of gravitationally dominated hydrostatic balance. For the case of a baroclinic fluid, the Taylor–Proudman theorem states that this rotation profile must be cylindrical, ie, with isorotation contours that align with the axis. TWB considers the case where deviations from the Taylor–Proudman profile are caused by baroclinic forcing (ie, vorticity due to misaligned density and pressure gradients).

We now show that we can recover the TWB equation from the G–S equation in the hydrodynamic limit by neglecting the poloidal flow. In this limit, the PDE (2.18) and Bernoulli equation (2.17) become the following:

$$\frac{\mathcal{L}^{2\prime}}{2\lambda^2} + \frac{1}{\gamma - 1}\frac{p}{\rho}\sigma' - H' = 0, \tag{4.1}$$

$$\frac{\mathcal{L}^2}{2\lambda^2} + \frac{\gamma}{\gamma - 1}\frac{p}{\rho} + \Phi - H = 0, \tag{4.2}$$

where $\mathcal{L} \equiv L/\chi' = \Omega\lambda^2$, $\Omega \equiv v_\phi/\lambda$, and primes denote partial derivatives with respect to ξ. We remark that $\mathcal{L}$ is simply the specific angular momentum, and Ω is the rotation rate.

We take the derivative of equations (4.1) and (4.2) along the stream surfaces, ie, in the direction of $\underline{\mathbf{X}} \equiv \underline{\nabla}\phi \times \underline{\nabla}\xi$. To simplify the expressions, note the following:

$$\begin{aligned}
&\underline{\mathbf{X}}\cdot\underline{\nabla}\lambda^2 = 2\frac{\partial\xi}{\partial z},\\
&\underline{\mathbf{X}}\cdot\underline{\nabla}r = -\frac{1}{\lambda r}\frac{\partial\xi}{\partial\theta},\\
&\underline{\mathbf{X}}\cdot\underline{\nabla}f = 0 \quad \forall f \in \{\xi, \psi, \chi, F, L, \text{Ł}, \sigma, H\}\,.
\end{aligned}$$

Then, we evaluate $\underline{\mathbf{X}} \cdot \underline{\nabla}$ of equation (4.2):

$$\begin{aligned}
\frac{\gamma}{\gamma-1}\underline{\mathbf{X}}\cdot\underline{\nabla}\frac{p}{\rho} &= -\underline{\mathbf{X}}\cdot\underline{\nabla}\frac{\text{Ł}^2}{2\lambda^2} - \underline{\mathbf{X}}\cdot\underline{\nabla}\Phi + \underline{\mathbf{X}}\cdot\underline{\nabla}H\\
&= \frac{\text{Ł}^2}{\lambda^4}\frac{\partial\xi}{\partial z} + \frac{g}{\lambda r}\frac{\partial\xi}{\partial\theta},
\end{aligned} \tag{4.3}$$

where $g(r) = d\Phi(r)/dr$ is the gravitational force.

In the hydrostatic limit, gravity dominates centrifugal terms; assuming $\partial\xi/\partial z \lesssim \partial\xi/\partial\theta$, the first term on the right side of equation (4.3) is $\mathcal{O}(\lambda\Omega^2/g) \ll 1$ compared to the second. The TWB equation is obtained by substituting equation (4.3) into $\underline{\mathbf{X}} \cdot \underline{\nabla}$ of equation (4.1):

$$\underline{\mathbf{X}}\cdot\underline{\nabla}\frac{\text{Ł}^{2\prime}}{2\lambda^2} = \underline{\mathbf{X}}\cdot\underline{\nabla}H' - \frac{1}{\gamma-1}\underline{\mathbf{X}}\cdot\underline{\nabla}\frac{p\sigma'}{\rho} \tag{4.4}$$

$$\Rightarrow \frac{\partial\Omega^2}{\partial z} = \frac{g}{\gamma\lambda r}\frac{\partial\sigma}{\partial\theta}\left[1 + \mathcal{O}\left(\frac{\lambda\Omega^2}{g}\right)\right]. \tag{4.5}$$

Hence, we have derived the TWB equation by taking the appropriate limit of the HD G–S equation.

Note that there is no reference to stream surfaces in equation (4.5). Indeed, the case of zero poloidal flow is a singular limit, as the equations that constrained Ł and σ to be constant along stream surfaces (eg, $\underline{\mathbf{v}} \cdot \underline{\nabla}\sigma = 0$) are trivially satisfied. Thus, the two scalar

variables, Ω and σ, are only required to satisfy the single equation (4.5), and the problem is underdetermined.

In [6], Balbus considered closing this TWB model by assuming the alignment of rotation and entropy contours (ie, $\sigma = \sigma(\Omega)$), thus obtaining a system where a choice of the rotation and entropy on the surface can be uniquely extrapolated into the interior. This assumption is strikingly similar to the appearance of stream surfaces in the G–S formalism (when $|\underline{\mathbf{v}}_{\mathrm{p}}| > 0$); since $Ł$ and σ are both functions of ξ, this implies that $\sigma = \sigma(Ł)$.

It should be noted that Balbus [6] considered this σ–$Ł$ alignment as well, but subsequently focused only on the σ–Ω assumption due to a perceived stronger qualitative agreement with CZ observations. However, as shown in Figure 4.1, this apparent advantage arises from the difference in the choice of the entropy profile at the surface, not from the effect of the σ–Ω alignment. When the two choices of entropy closure are put on equal footing (ie, with the same rotation and entropy at the surface), we find that both do equally well in capturing the characteristic rotation in the CZ.

Thus, we consider this relatively unexplored σ–$Ł$ alignment as the natural limit of axisymmetric fluid equilibrium with vanishing poloidal flows, and using this framework, we evaluate the effects of including a nonzero poloidal flow on the rotation profile.

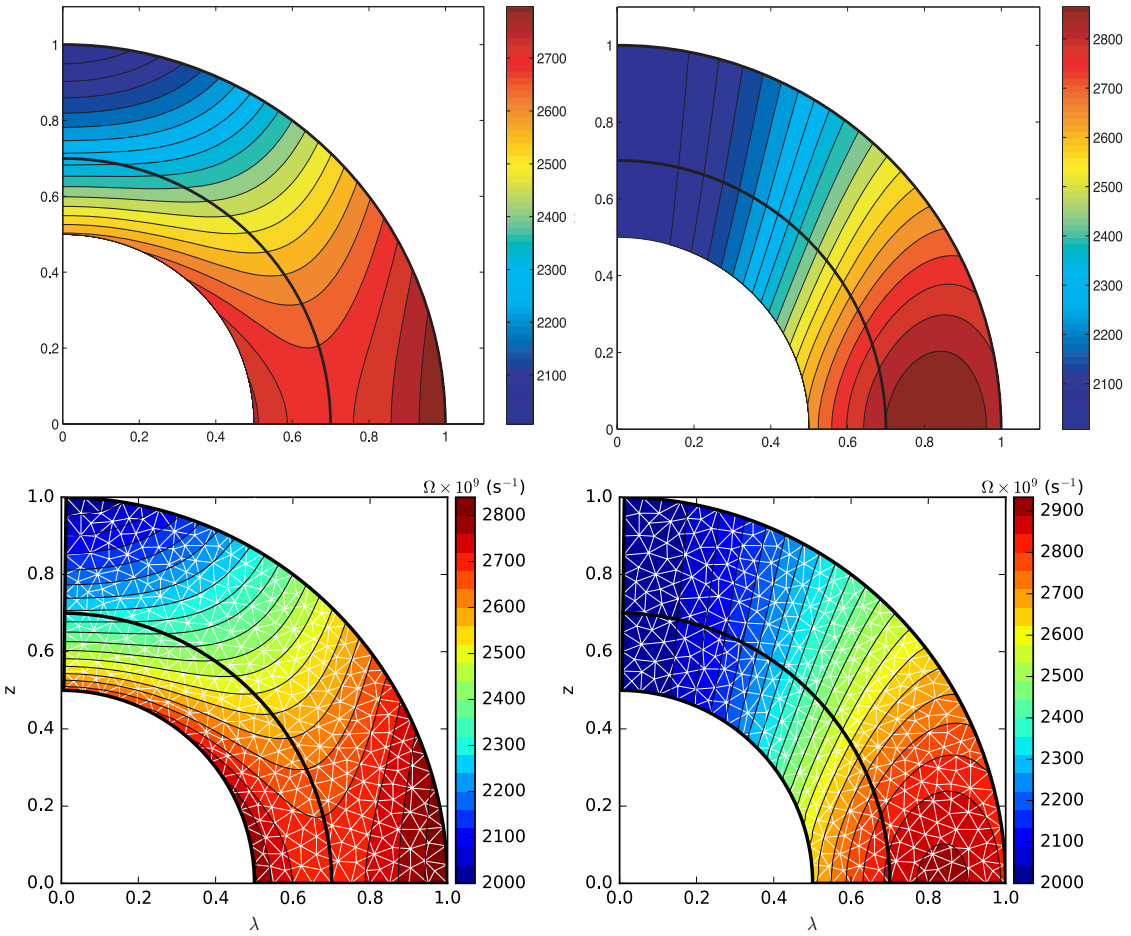

Figure 4.1: **The choice of latitudinal entropy gradient is much more relevant than the choice of entropy alignment for modeling the CZ.** *Top* figures show rotation profiles of TWB solutions from Balbus [6]. *Top left*: Using σ–Ω alignment. *Top right*: Using σ–$\mathcal{L}$ alignment. In both cases, rotation at the surface was chosen to match solar observations, but the functional form of the entropy is prescribed as $\sigma \propto -\Omega^2$ and $\sigma \propto -\mathcal{L}^2 = -\Omega^2\lambda^4$, respectively. The gradient of the latter function occurs at a larger cylindrical radius, λ, resulting in a lack of tilting of contours at mid to high latitudes and overly tilted contours near the equator. *Bottom* figures shows our results from Grad–Shafranov theory (ie, both with the σ–$\mathcal{L}$ alignment), where rotation and entropy at the surface are chosen to match those immediately above.

4.5 Comparison with observations

We have demonstrated that we can recover the qualitative features of the CZ rotation profile with our G–S model, but what about quantitatively? In [7], Balbus considered a more general form of rotation and entropy as a function of latitude, fitting the profiles to match the value and angle of the isorotation contours in the bulk of the CZ, and obtained a good agreement away from the surface and tachocline. Likewise, by exploiting the freedom in the form of the stream functions, we obtain an equally striking fit to helioseismology data, as shown in Figure 4.2.

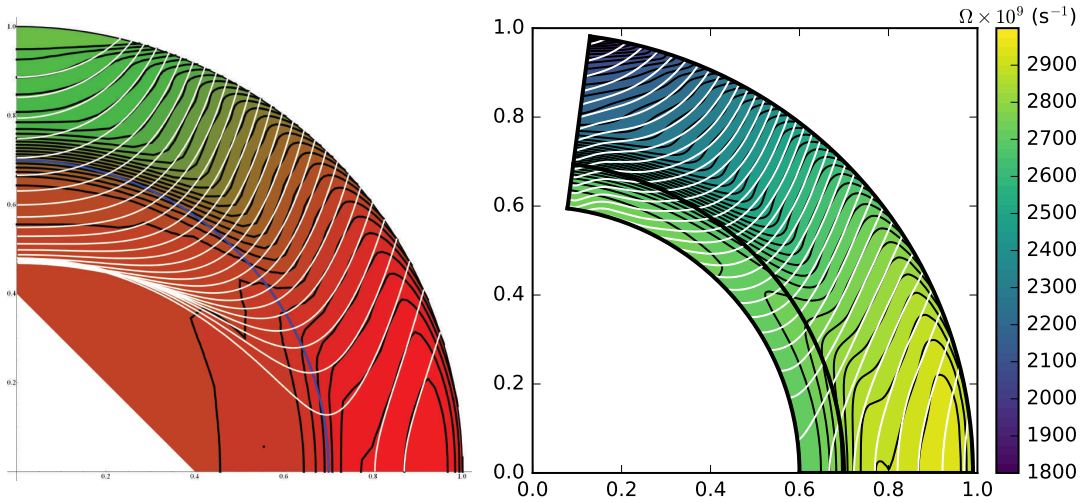

Figure 4.2: **Models of thermal wind balance can replicate observations in the CZ (away from the surface and the tachocline).** *Left*: Best fit from Balbus [7] is shown in white, and helioseismic data in black. *Right*: Best fit from our G–S model is shown in white, and data helioseismic from [55] in black.

4.6 Incorporating residual entropy

In [7], Balbus also introduced a slightly more general σ–Ω connection by dividing the entropy into a spherically symmetric part and an aspherical part, positing that the latter

"residual entropy" aligns with rotation, giving $\sigma = \sigma_r(r) + \sigma_\Omega(\Omega)$. Their motivations were twofold: first is the mathematically convenient fact that TWB (equation (4.5)) is insensitive to this radial entropy profile, so the form of their solution is unchanged; and second is that convection in the absence of rotation would be in dynamic equilibrium with a superadiabatic radial entropy gradient, so the aspherical effects of rotation should be considered with respect to this spherically symmetric state. Indeed, simulations in [66] found that isorotation contours are better aligned with this residual entropy than with the total entropy. We now demonstrate how a similar entropy assumption can fit into the framework of the G–S equation.

In the derivation of equations (2.17) and (2.18), the assumption of stationary adiabatic flows implies that entropy is a stream function $\underline{\mathbf{v}} \cdot \underline{\nabla}\sigma = 0 \Rightarrow \sigma = \sigma(\xi)$. This assumption clearly does not hold in the Sun, where heat transport is dominated by radiation and turbulent convection (instead of mean-flow advection). However, our motivations for using this adiabatic closure are likewise twofold: theoretical, because such a closure allows one to use the techniques of global MHD equilibrium and stability; and practical, because the particular choice of closure matters much less than the overall latitudinal entropy profile (a free parameter in both models).

Yet, as the radial entropy stratification is not small compared to the putative latitudinal gradient, it behooves us to separate out a spherically symmetric component. Thus, in the spirit of Balbus [7], we assume the following form for the entropy:

$$\sigma = \langle\sigma\rangle + \sigma_r(r) + \sigma_\xi, \qquad \mathbf{v} \cdot \underline{\nabla}\sigma_\xi = 0, \tag{4.6}$$

so that the *residual* entropy, $\sigma_\xi = \sigma_\xi(\xi)$, is a stream function.

We now trace the effects of this more general entropy assumption on the derivation of the Bernoulli equation ((2.17)) and G–S PDE ((2.18)). For simplicity, we will outline the

results for the HD limit, as the results are the same for the general MHD case. The pressure term of equation (2.3) in the direction of $\underline{\mathbf{v}}$ becomes

$$\begin{aligned}\rho^{-1}\underline{\mathbf{X}}\cdot\underline{\nabla}p &= \rho^{-1}\underline{\mathbf{X}}\cdot\underline{\nabla}\left[e^{\langle\sigma\rangle+\sigma_r+\sigma_\xi}\rho^\gamma\right] \\ &= -\frac{1}{\gamma-1}\frac{p}{\rho}\underline{\mathbf{X}}\cdot\underline{\nabla}\sigma_r + \underline{\mathbf{X}}\cdot\underline{\nabla}\left(\frac{\gamma}{\gamma-1}\frac{p}{\rho}\right).\end{aligned}$$

The second term here yields the same entropy term as in equation (2.17), while the first term can be approximately absorbed into a modified radial gravitational potential:

$$\underbrace{\frac{1}{2}\frac{\chi'^2\left|\underline{\nabla}\xi\right|^2}{\rho^2\lambda^2}+\frac{1}{2}\frac{L^2}{\chi'^2\lambda^2}+\frac{\gamma\rho^{\gamma-1}}{\gamma-1}e^\sigma+G_\mathrm{m}-H}_{\text{modified Bernoulli equation}} = \underbrace{\int\frac{\delta T}{\gamma-1}\underline{\mathbf{X}}\cdot\underline{\nabla}\sigma_r\frac{dl}{|\underline{\mathbf{X}}|}}_{\mathcal{O}(\sigma_r\delta T)}, \tag{4.7}$$

where the integral is taken along the relevant stream surface, the modified gravitational potential is

$$G_\mathrm{m}(r) = G(r) - \frac{1}{\gamma-1}\int^r\frac{p_0}{\rho_0}\frac{d\sigma_r}{dr}dr, \tag{4.8}$$

and the temperature perturbation is $\delta T \equiv p/\rho - p_0/\rho_0$. The quantities p_0 and ρ_0 are the background radial pressure and density profiles, which satisfy hydrostatic balance:

$$\rho_0(r) = \left(\frac{\gamma-1}{\gamma}\frac{\langle H\rangle - G(r)}{e^{\langle\sigma\rangle+\sigma_r(r)}}\right)^{\frac{1}{\gamma-1}}, \tag{4.9}$$

$$p_0(r) = \rho_0^\gamma e^{\langle\sigma\rangle+\sigma_r}, \tag{4.10}$$

where angled brackets denote a mean value (note that $H - \langle H\rangle \ll \langle H\rangle$ in the solar case).

In obtaining the PDE ((2.18)), the pressure and gravity terms in the momentum equation ((2.3)) are canceled by terms from $\rho\underline{\nabla}$ of equation (2.17). Consider the corresponding

terms in $\rho\underline{\nabla}$ of equation (4.7):

$$\begin{aligned}\rho\underline{\nabla}H &= \rho\underline{\nabla}G_{\mathrm{m}} + \frac{\gamma}{\gamma-1}\rho\underline{\nabla}\left(\frac{p}{\rho}\right) + \cdots \\ &= \underbrace{\rho\underline{\nabla}G + \underline{\nabla}p}_{\text{cancels with equation (2.3)}} + \underbrace{\frac{1}{\gamma-1}p\underline{\nabla}\sigma_\xi}_{\text{term in PDE ((2.18))}} + \underbrace{\frac{1}{\gamma-1}p\frac{\delta T}{T}\underline{\nabla}\sigma_r}_{\mathcal{O}\left(\sigma_r\frac{\delta T}{T}p\right)} + \cdots .\end{aligned}$$

Thus, both the PDE and the Bernoulli equation are changed by terms of size $\mathcal{O}(\sigma_r\delta T/T)$, which is much smaller than the dominant balance of size $\mathcal{O}(\sigma_\xi)$ between differential rotation and residual entropy. Indeed, the radial entropy profile is only weakly superadiabatic in the CZ; from mixing-length arguments, the change in entropy over a pressure scale height is $\sim 10^{-7}$ at the base and $\sim 10^{-2}$ at $\sim 0.5\%$ below the surface [62], so $\sigma_\xi \lesssim \sigma_r \ll 1$. If differential rotation is driven primarily by baroclinic forcing, then $\delta T/T \sim \sigma_\xi \ll 1$, so this $\mathcal{O}(\sigma_r\delta T/T)$ term can be dropped. However, this term may not be negligible in the radiative interior (where σ_r is strongly subadiabatic) or at the surface (where $\rho \to 0$). Indeed, both our model (at least as is, but see Chapters 5 and 6) and that of Balbus break down in these regions.

What have we gained by demonstrating the insensitivity of our model to a radial entropy profile? Using data from the 3D CZ simulations of Miesch et al. [66], Balbus [7] subtracted a particular choice of radial profile to show that the residual entropy can be made to align with rotation. Here, we show that a different choice can be made to align it with angular momentum. To demonstrate this, we add a radial profile that aligns our model's total entropy with rotation, as seen in Figure 4.3. Thus, by subtracting this radial profile, Balbus's relationship between rotation and residual entropy can be transformed into a relationship between angular momentum and a different choice of residual entropy.

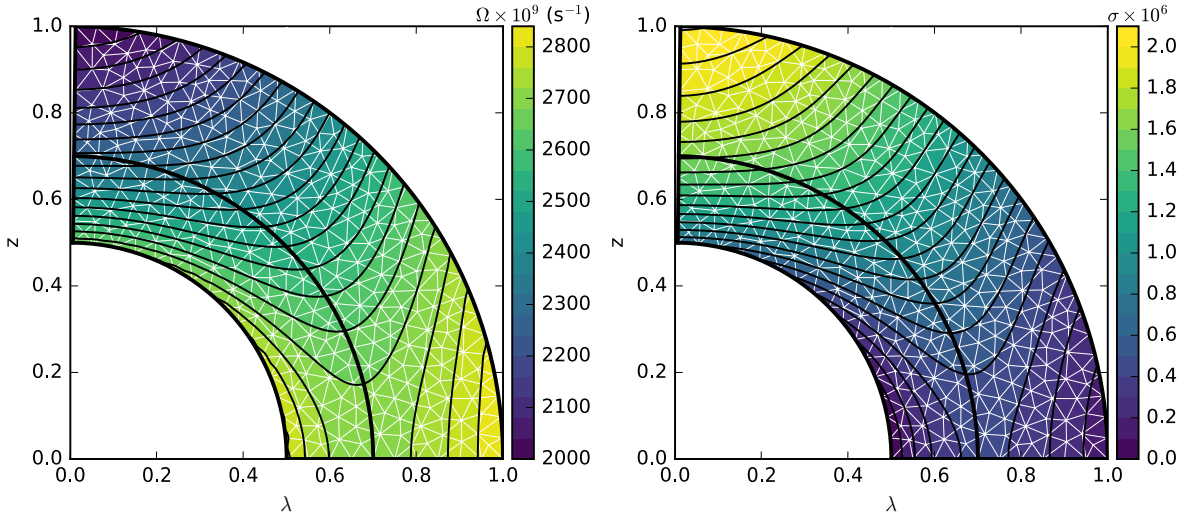

Figure 4.3: **The freedom afforded by the choice of radial entropy allows our model to mimic the σ–Ω alignment.** *Left*: Isorotation contours. *Right*: Entropy contours ($\sigma = \sigma_r(r) + \sigma_\xi(\xi)$).

4.7 Discussion

In this chapter, we employed the hydrodynamic limit of the Grad–Shafranov equation to obtain gravitationally dominated equilibrium states with a solar-like differential rotation. In this limit, the surfaces of constant entropy align with those of angular momentum. We compared results from our model to those with the entropy–rotation alignment of Balbus [6], finding an equally good agreement with helioseismic observations.

Similar to Balbus [7], we demonstrated that it is possible to introduce a small radial entropy gradient while leaving the form of the equilibrium equations unchanged to leading order. With the freedom afforded by this arbitrary radial profile, we showed that an aspherical entropy aligned with angular momentum can be changed into one that is nearly aligned with rotation. Thus, the numerical simulations that demonstrate an alignment of aspherical entropy with rotation [7] could just as well support an alignment with angular momentum by using a different choice of spherical entropy gradient. Compared to the superadiabatic

gradient driving convection, these choices of spherical entropy gradient become comparable only near the base.

Chapter 5

The Near Surface Shear Layer

In this chapter, we consider the inclusion of poloidal flow in the generalized G–S equation (still in the hydrodynamic limit). While this modification does not introduce any qualitative changes in our results for the rotation profile of the convection zone, the limit of vanishing density at the surface leads to a slowing of rotation at the surface. This decrease in surface rotation found in our model qualitatively similar to that found in the NSSL.

5.1 Characteristics of the NSSL

The first evidence for the NSSL was the observation that emerging active regions rotate at a rate faster than that of the surrounding photosphere [30]. The conventional explanation for its existence is the effective mixing of angular momentum due to strong convective flows in the outer layers [21, 68].

In slowly rotating objects, the radial motion of convection effectively advects angular momentum radially inward [68]. In contrast, in strongly rotating objects, Coriolis forces constrain these convective motions to form coherent structures aligned with the rotation

axis, resulting in Reynolds stresses that transport angular momentum outward (see [16] and Section 4.1.2). It appears that the relevant parameter is the convective Rossby number, ie, the ratio of the rotation period and the convective timescale, $\text{Ro} = k|\underline{\mathbf{v}}_c|/2\Omega$, where k is the inverse lengthscale of convection, $|\underline{\mathbf{v}}_c|$ is the characteristic velocity of convection, and Ω is the bulk rotation rate. Indeed, Gastine et al. [32] conducted a large parameter scan of rotating convection simulations, finding that this convective Rossby number is a good indicator of whether an object will exhibit solar-like (fast equator and slow poles, when $\text{Ro} \lesssim 1$) or anti-solar (slow equator and fast poles, when $\text{Ro} \gtrsim 1$) rotation.

However, the same object can exhibit both types of rotation. For example, while the majority of the solar interior likely exhibits rotationally-constrained convection ($\text{Ro} \lesssim 1$), the outer layers probably operate in the opposite regime. Indeed, as one approaches the surface of the Sun, relative density and pressure gradients become more pronounced, and convection becomes more vigorous, reaching velocities on the order of the sound speed. As convection is no longer rotationally-constrained, conservation of angular momentum suggests a decrease in rotation rate as a function of cylindrical radius in these outer layers, as is observed in the solar data and recovered in high-resolution simulations of convection in this region [54].

We now extend our equilibrium description of the solar rotation profile by including a weak poloidal flow, considering in particular its effects on the equilibrium close to the solar surface.

5.2 Robustness to weak poloidal flows

In Chapter 4, we neglected the terms in equation (2.18) representing the effects of poloidal flows (or, more precisely, considered the $|\underline{\mathbf{v}}_p| \to 0$ limit), leading to an algebraic equation that uniquely determined the solution. Thus, there was no need to specify boundary condi-

tions. However, when poloidal terms are included, the resulting PDE has a continuum of possible solutions, corresponding to different choices of boundary conditions.

To qualitatively understand the effect of a nonzero poloidal flow, we split the PDE (2.18) into a "differential term" $\Delta^\star$, which contains all the terms that depend on spatial derivatives of ξ, and an "algebraic term" A, which contains everything else:

$$\underbrace{\underline{\nabla}\cdot\left[\left(\psi'^2-\frac{\chi'^2}{\rho}\right)\frac{\underline{\nabla}\xi}{\lambda^2}\right]-\frac{1}{2}\left(\psi'^2-\frac{\chi'^2}{\rho}\right)'\frac{|\underline{\nabla}\xi|^2}{\lambda^2}}_{\text{“differential term” }\Delta^\star[\xi]}$$
$$+\underbrace{\left[\left(\frac{L^2}{2\lambda^2}+\frac{\chi' LF}{\psi'}+\frac{\rho\lambda^2F^2}{2}\right)\Big/\left(\psi'^2-\frac{\chi'^2}{\rho}\right)-\frac{1}{\gamma-1}\rho^\gamma e^\sigma+\rho H\right]'}_{\text{“algebraic term” }A(\xi,\rho,\lambda)}=0. \tag{5.1}$$

In the bulk of the CZ, we expect the "differential term" to be about $\underline{\mathbf{v}}_\mathrm{p}^2/v_\phi^2\lesssim 10^{-4}$ times smaller than the "algebraic term". We then linearize equation (5.1) about the TWB solution ξ_TWB, satisfying $A(\xi_\mathrm{TWB},\rho_0,\lambda)=0$, and search for time-independent ($\omega=0$) perturbations, giving a family of nearby equilibria.

First, we fix a background hydrostatic density profile, $\rho_0(r)$. We consider a nearby smooth solution, ξ_0, that satisfies equation (5.1),

$$\Delta^\star[\xi_0]+A(\xi_0,\rho_0,\lambda)=0. \tag{5.2}$$

Because the scale length of ξ_TWB is similar to the size of the CZ, the "differential term" is indeed a small parameter, and ξ_0 will not differ from ξ_TWB significantly. However, if we consider a short-wavelength perturbation to this solution, the "differential term" can become comparable. The linearized equation for a perturbation $\xi_1=\xi-\xi_0$ is

$$\delta\Delta^\star[\xi_0;\xi_1]+\xi_1\left.\frac{\partial A}{\partial\xi}\right|_{\xi=\xi_0}=0, \tag{5.3}$$

where $\delta\Delta^\star[\xi_0;\xi_1]$ is the functional derivative of $\Delta^\star$ with respect to ξ_1, evaluated at ξ_0.

Let ξ_1 be a local perturbation of the form $\exp(i\underline{\mathbf{k}}\cdot\underline{\mathbf{x}})$, so that $\underline{\nabla}\xi_1 \sim i\underline{\mathbf{k}}\xi_1$ and $\nabla^2\xi_1 \sim -k^2\xi_1$. By keeping only terms with at least one power of $\underline{\mathbf{k}}$, the linearized differential operator becomes

$$\delta\Delta^\star[\xi_0;\xi_1] \approx \frac{\chi'^2 k^2}{\rho\lambda^2}\xi_1 - i\underline{\mathbf{k}}\cdot\underline{\nabla}\left(\frac{\chi'^2}{\rho\lambda^2}\right)\xi_1. \tag{5.4}$$

Equations (5.3) and (5.4) give a local dispersion relation,

$$k^2 + i\underline{\mathbf{k}}\cdot\underline{\nabla}\ln\left(\frac{\rho\lambda^2}{\chi'^2}\right) \approx \frac{\chi'^2|\underline{\nabla}\xi|^2 A'}{\rho\underline{\mathbf{v}}_{\mathrm{p}}^2} \equiv K^2. \tag{5.5}$$

We note that K is real, as in the hydrodynamic limit with strong rotation, the sign of A' is given by the change in angular momentum as a function of cylindrical radius, and so $A' \geq 0$ for solar-like rotation (ie, fast equator and slow poles).

We identify two limiting cases of this relation:

$$k^2 \approx K^2, \qquad \text{if} \quad \left|\underline{\nabla}\ln\left(\frac{\rho\lambda^2}{\chi'^2}\right)\right| \ll K, \tag{5.6}$$

$$i\underline{\mathbf{k}}\cdot\underline{\nabla}\ln\left(\frac{\rho\lambda^2}{\chi'^2}\right) \approx K^2, \qquad \text{if} \quad \left|\underline{\nabla}\ln\left(\frac{\rho\lambda^2}{\chi'^2}\right)\right| \gg K. \tag{5.7}$$

Let us evaluate K^2 for parameters relevant to the solar CZ. To obtain A', we note that the stream surfaces are nearly cylindrical ($\xi \approx \xi(\lambda)$), and differentiate $A = 0$ with respect to ξ at constant ρ:

$$\left(\frac{\partial A}{\partial \xi}\right)\bigg|_\rho = \frac{\partial A}{\partial \xi} + \frac{\partial A}{\partial \lambda}\frac{\partial \lambda}{\partial \xi} = 0$$
$$\implies A' \approx -\frac{\partial A}{\partial \lambda}\frac{d\lambda}{d\xi} = \rho\frac{d\lambda}{d\xi}\frac{\mathcal{L}^{2\prime}}{\lambda^3} \approx \frac{\rho}{\lambda^3}\left(\frac{d\lambda}{d\xi}\right)^2\frac{d}{d\lambda}\left(\lambda^4\Omega^2\right).$$

Then K^2 is given by

$$K^2 \approx \frac{1}{\underline{\mathbf{v}}_{\mathrm{p}}^2} \frac{1}{\lambda^3} \frac{d}{d\lambda} \left(\lambda^4 \Omega^2 \right) . \tag{5.8}$$

In the Sun, $K^2 > 0$, and (in the regions away from the surface and rotation axis) the first limit (equation (5.6)) is applicable. Thus, in the bulk of the CZ, deviations from TWB take the form of sinusoidal perturbations around ξ_0, with a wavelength that is inversely proportional to the density, $k^{-1} \sim K^{-1} \propto |\underline{\mathbf{v}}_{\mathrm{p}}| \propto \rho^{-1}$. Equation (5.8) suggests an interpretation of these perturbations as the epicyclic motion of a fluid element, traced out in space via advection by the poloidal flow.

Numerically, we first solve equation (5.2) for the smooth TWB solution in a small section of the CZ, then add a perturbation to the gradient on the upper boundary. Figure 5.1 shows the results of this procedure for three different sections of the CZ, with increasing depths from left to right, demonstrating that the wavelength of the perturbations decreases consistent with equation (5.8). Because the wavelength of these perturbations is small ($\sim 0.001 R_\odot$ at $r = 0.9 R_\odot$), any significant deviation from the smooth solution in the CZ would result in large-amplitude, oscillatory gradients in the rotation. Even if these structures could be resolved by observations, they are likely to be suppressed (eg, due to turbulent viscosity from convective motions). Thus, in the bulk of the CZ, we expect to see the smooth TWB solution.

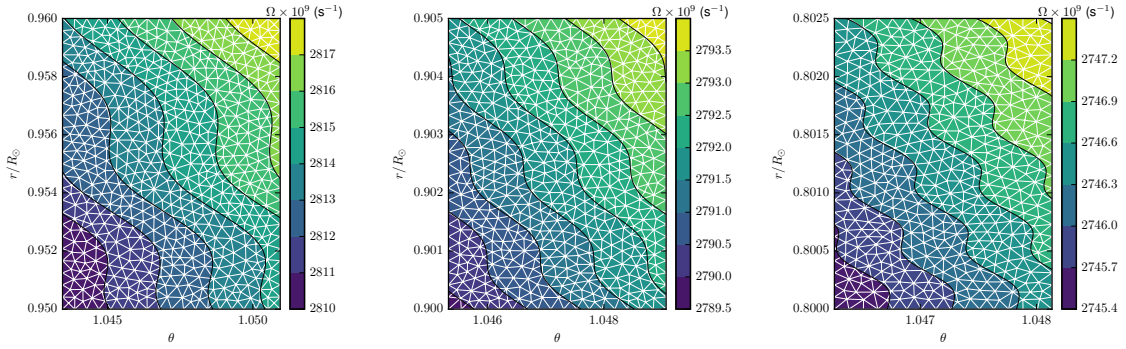

Figure 5.1: **Short wavelength epicyclic oscillations around the smooth TWB solution in the CZ.** A perturbation to the gradient is applied to the upper boundary, and nonreflecting boundary conditions (see Section 3.2.2) are applied to the sides and bottom. The figures display isorotation contours in a small section at 30° above the equator at decreasing radii from left to right: $r/R_\odot = 0.95, 0.9, 0.8$. Note the size of the domain; the perturbations have a short wavelength, consistent with equation (5.8).

5.3 Equilibrium NSSL

Near the surface, the "differential term" of the PDE (5.1) is no longer subdominant, qualitatively changing the smooth solution ξ_{TWB} (equation (5.2)). Hydrostatic balance suggests that the density decreases to zero as $\rho(r) \propto (R_\odot - r)^{\frac{1}{\gamma-1}}$. Hence, $\nabla \ln \rho$ diverges radially and $K^2 \to 0$, so we are in the second limit (equation (5.7)). The dominant balance is now given by

$$\frac{\partial \xi}{\partial r} - \frac{K^2}{\frac{d}{dr} \ln \rho} \xi_1 \approx 0. \tag{5.9}$$

Thus, $\partial \xi / \partial r \to 0$, so the cylindrical stream surfaces in the CZ become oriented radially as they approach the surface. As angular momentum is constant along stream surfaces, this corresponds to a slowing of the rotation at the surface, as seen in Figure 5.2. This transition

occurs when the density scale height, $|\nabla \ln \rho|^{-1}$, becomes comparable to the wavelength given by equation (5.6), which occurs in the outer $\sim 2\%$ the solar surface.

While the effects of this transition are qualitatively similar to the near surface shear layer in the Sun, the location is confined much closer to the surface, so hydrodynamic equilibrium is suggestive but insufficient as an explanation for the NSSL.

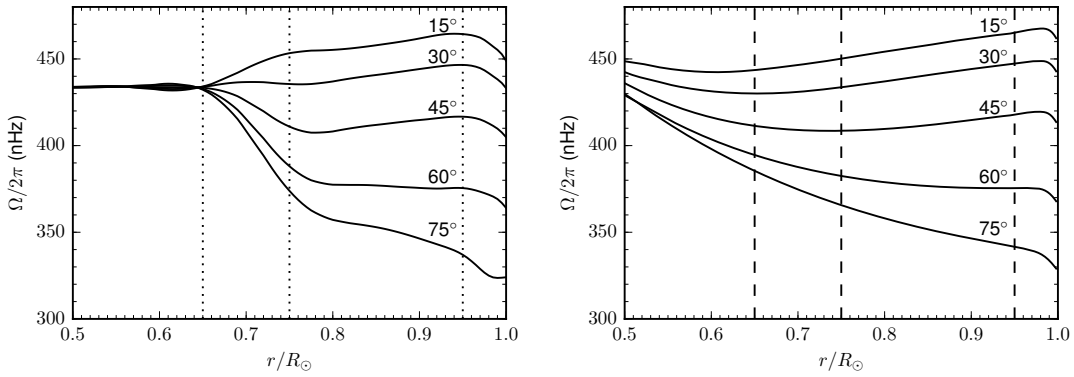

Figure 5.2: **The inclusion of a poloidal flow results in a qualitative NSSL.** *Left:* Rotation as a function of radius for several latitudes, as obtained by helioseismology (data from [55]). Dashed lines at $0.65R_\odot$, $0.75R_\odot$, and $0.95R_\odot$ provide approximate divisions between the radiative interior, tachocline, CZ, and NSSL. *Right:* The same plot for our hydrodynamic Grad-Shafranov model, with $\rho = 1$ kg m^{-3} and $\mathrm{v_p} = 20$ m s^{-1} at $r = 0.99R_\odot$. The profile shows a decrease in rotation near the surface that is qualitatively similar to the NSSL in the Sun, albeit occurring in a region that is a factor of ~ 3 smaller. One notable feature missing from our profile is the transition to uniform rotation at the tachocline. However, there are two reasons to believe that magnetic effects could become important at this layer and below: poloidal flows become weaker as the convective driving is suppressed in these stably stratified regions, and the effects of a putative interior fossil field could enter the equilibrium at lowest order (see Chapter 6).

5.4 Discussion

In this chapter, we allowed for a weak poloidal flow and considered its effects on the equilibrium profile given by the hydrodynamic limit of the G–S equation (for parameters relevant to the solar regime).

In the convection zone, perturbations around this smooth solution appear with a wavelength inversely proportional to the density. These epicyclic oscillations are much shorter than the length scale of the background solution ($\sim 0.01 R_\odot$ at $r \sim 0.97 R_\odot$, decreasing to $\sim 0.001 R_\odot$ at $r \sim 0.9 R_\odot$). Thus, the addition of a solar-relevant poloidal flow does not significantly change the equilibrium profile in the bulk of the convection zone, suggesting that the equilibrium in this region is stiff to perturbations by the boundary. However, while the solution in the bulk of the CZ was relatively unchanged, a decrease in the rotation appears within $\sim 2\%$ of the solar surface, reminiscent of the near surface shear layer, albeit distinctly smaller.

In the next chapter, we investigate the effects of including a magnetic field, and its putative relationship with the Tachocline. In contrast to flow velocities that decrease with depth, magnetic fields have an increasing effect on the equilibrium profile. Indeed, magnetism has been suggested as essential to understanding the tachocline and radiative interior [39, 84, 85, 104], and cyclic variations in the mean flows are likely intertwined with the solar magnetic cycle [97, 79, 12]. In addition, surface measurements of poloidal field and flow indicate the possibility of an Alfvénic transition layer at this depth, which could lead to steep gradients qualitatively similar to a tachocline.

Chapter 6

The Tachocline

Everyone forgets Icarus also flew.

—— Jack Gilbert, *Refusing Heaven*

In this chapter, we include both toroidal and poloidal fields and flows, studying the full G–S equation for solar-relevant parameters. In Section 6.3, we present a global solution that (smoothly) crosses the Alfvén surface and associated hyperbolic layer. While the global solutions leave these layers unresolved, we justify these smooth solutions using a 1D linear analysis (Section 6.4.1). Moreover, by iteratively zooming in on the transition, we obtain resolved local equilibria consistent with the smooth global solutions. After exploring the space of smooth equilibria (Section 6.5), we then consider the interaction between the short wavelength oscillations from Chapter 5 and the Alfvén surface (Section 6.6). The smooth equilibria appear to not be robust to perturbations, opening the possibility for a "weak tachocline hypothesis", discussed at the end of this chapter (Section 6.7).

6.1 Characteristics of the Tachocline

6.1.1 Basic properties

The primary revelation of cylindrical helioseismology (see Chapter 1 Section 1.4.2) is arguably the sharp radial gradient in rotation at the base of the Convection Zone. This transition is known as the Tachocline, and the reasons for its narrowness remain enigmatic.

The observation of such a region sparked renewed interest in Babcock–Leighton models of the solar cycle, which require a source of internal shear to amplify toroidal fields from poloidal fields via the ω-effect [4]. The precise nature of the rotational coupling across this layer is also important for stellar spin-down models, and the circulation patterns induced by this region are likewise of great interest to models of compositional mixing in the Sun. However, these models typically enforce the existence of such a transition layer, eg, by a prescribed rotation profile [24, 18] or a particular choice of boundary conditions [66]. There are still many open questions: Why is the transition so narrow? How does the interior "decouple" itself from the outer layers, so as to rotate essentially uniformly? And if the interior is so decoupled, why is it rotating at nearly the current mean solar rate, instead of $\sim 10\times$ faster (as it was when the Sun was formed)?

Spiegel [89] was the one to coin the term "tachocline". He argued that the stable stratification and strong radial shear in this transition region would result in anisotropic turbulence, which would act as a strong horizontal viscosity, thereby homogenizing the rotation. However, there is no agreement on what sort of instabilities could drive this putative turbulence. Moreover, the nature of horizontal turbulence in such systems may drive them *away* from uniform rotation, instead mixing potential vorticity and acting in an "anti-frictional" way [64]. And even if such a preferential horizontal mixing were to provide such an anisotropic friction, it still leaves unanswered the question of why there is nearly no radial shear in the Radiative Interior; if radial motions are suppressed, how does the CZ

communicate its average rotation to the radially decoupled interior? Several studies have invoked gravity waves as a mechanism for transporting angular momentum to the interior [94], but this has likewise been shown to act in an "anti-frictional" manner [81].

6.1.2 Gough and McIntyre model and subsequent simulations

Motivated by these issues with a purely hydrodynamical description, Gough & McIntyre [39] claimed that there must be a large scale magnetic field in the solar interior. They performed a boundary layer analysis by considering the competition between an outwardly diffusing poloidal field in the Radiative Interior and a downward poloidal flow from the Convection Zone. Then, by comparing with the thickness of the Tachocline, they concluded that a $\sim 10^{-4}$ T field could hold the interior in uniform rotation. This amplitude is consistent with the idea of a "fossil field", ie, the concentration of a background magnetic field during the Sun's initial formation.

However, subsequent simulations of the Gough & McIntyre model of the Tachocline (GM98) have found that such a delicate balance between field and flow is difficult to obtain in practice [105, 104, 3]. In general, simulations find that the interior poloidal field quickly diffuses into the Convection Zone. Then, by Ferraro's theorem of isorotation [28], which states that rotation is uniform along a poloidal field line, the differential rotation of the CZ is efficiently communicated to the interior. The question then becomes: how could the interior field be contained against such outward diffusion?

Acevedo-Arreguin et al. [3] described the first global simulation of the GM98 model, proposing an explanation for the fact that previous simulations of this model could not contain this interior field. In particular, they considered an axisymmetric and steady-state model, with parameterized diffusion coefficients as a function of radius. They drove differential rotation in the upper CZ, maintaining the counterclockwise meridional circulation

via gyroscopic pumping, while the interior field was maintained by currents in the deep interior. They claimed that previous simulations failed because of an unrealistically large Prandtl number Pr, the ratio of momentum diffusivity and thermal diffusivity. This caused the downwelling meridional circulation to be viscously damped at the bottom of the CZ, thereby being unable to penetrate into the interior to confine the field. More precisely, the dimensionless parameter $\sigma \equiv \sqrt{\mathrm{Pr}}\left(\overline{N}/\Omega_\odot\right)$, which describes the relative importance of viscosity in the radiation zone, is $\sigma \gg 1$ in most simulations, despite the value being $\sigma < 1$ in and around the Tachocline. Thus, Acevedo-Arreguin et al. reduced Pr as low as possible, and then artificially reduced $\overline{N}/\Omega_\odot$ until $\sigma < 1$, indeed finding a GM98-like solution. In their simulations, the diffusivities are larger (and the rotation rate is smaller) than solar values, resulting in a tachocline that is much thicker than observations. However, their study of variations of these parameters within the computationally accessible regime suggests that the Tachocline should be appropriately narrow for solar parameters.

Comparing with our G–S model, one major difference is in the choice of heat transport. While these models balance entropy generation via adiabatic compression against thermal diffusion, both of these effects are outside the scope of the G–S equation. We are essentially considering purely advective transport, such that entropy is constant along flux/stream surfaces. Moreover, the appearance of GM98-like solutions seems to require a careful choice of radial diffusivity profiles, such that the smaller laminar magnetic diffusivity must extend slightly into the base of the Convection Zone, allowing for what is known as "pre-confinement". Although, as the magnitude of the diffusivities decreases towards solar-like values, such pre-confinement may not be necessary [3]. In contrast, our model has no Prandtl number and does not require carefully chosen diffusivity profiles (as both dissipations are by definition zero). Thus, it could shed light on this low-diffusivity regime.

6.2 Our "strong tachocline hypothesis"

Our strong tachocline hypothesis is that there exist solar-relevant equilibria that contain sharp discontinuities (or large gradients) associated with these Alfvén, slow, and cusp transitions, and that such features appear near the location of the Tachocline. The inclusion of a toroidal flow into the magnetostatic G–S equation presents no particular numerical difficulty; the resulting PDE remains elliptic everywhere. Likewise, including a toroidal field into the hydrodynamic G–S equation does not introduce any transitions in the regime we are considering (ie, subsonic flows). However, when *both* poloidal fields and flows are included, the structure of the PDE can change dramatically. The relevant parameter is the squared poloidal Alfvénic Mach number:

$$M_{AP}^2 \equiv \rho v_p^2 / B_p^2 = \chi'^2 / \rho \psi'^2. \tag{6.1}$$

Recall that the type of a PDE (elliptic, hyperbolic, or parabolic) is characterized by its discriminant. In our case, the discriminant can be written as

$$\Delta = \frac{\left(1 - M_{AP}^2\right)^2 \left(1 - \dfrac{\gamma p + B^2}{\gamma p} M_{AP}^2\right)}{\dfrac{B_p^2}{\gamma p} M_{AP}^4 - \dfrac{B^2}{\gamma p} M_{AP}^2 + 1}. \tag{6.2}$$

The discriminant changes sign when M_{AP}^2 passes through the critical values M_c^2, M_s^2, or M_f^2, corresponding to when the poloidal flow (projected along the field lines) matches the cusp, slow, and fast speeds, respectively (see Figure 6.1). It becomes zero (without changing sign) at $M_{AP}^2 = 1$ (the Alfvén point). In order of increasing poloidal flow: the PDE is elliptic ($\Delta > 0$) for $0 \leq M_{AP}^2 < M_c^2$, hyperbolic ($\Delta < 0$) for $M_c^2 < M_{AP}^2 < M_s^2$, elliptic for $M_s^2 < M_{AP}^2 < 1$ and $1 < M_{AP}^2 < M_f^2$, and again hyperbolic for $M_f^2 < M_{AP}^2$. At the Alfvén point ($M_{AP}^2 = 1$), the PDE becomes singular, reducing to an algebraic condition

that must be satisfied at this surface, and an application of l'Hôpital's rule gives a jump condition that connects the solutions on either side. Although the order of these critical points is always the same, the spacing between them can be quite different.

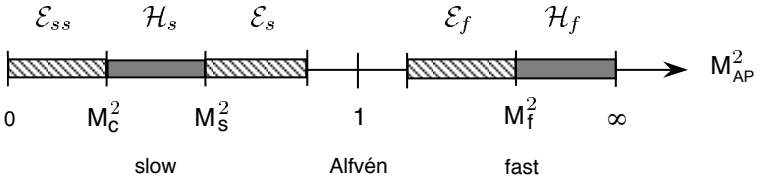

Figure 6.1: **Schematic of transitions in the generalized G–S equation** (image modified from [36]). The relevant transitions for solar equilibria are the Alfvén surface and both slow surfaces (the cusp and slow transitions). The fast surface is well outside the solar radius. When considering the G–S equation with translational invariance (such as in this schematic) there is a region around the Alfvén surface that is inaccessible to poloidal flows. However, in the rotationally invariant case (such as ours), this "forbidden region" collapses to zero width when a flux/stream surface is at a precise cylindrical radius, allowing for flows to continuously cross between $\mathcal{E}_s$ and $\mathcal{E}_f$. Moreover, for solar relevant parameters, $\mathcal{H}_s$ is incredibly narrow, and occurs very close to the Alfvén surface.

We adopt an ordering relevant to the solar regime, viz, $\beta \equiv \gamma p/B^2 \sim B/B_p \sim \mathcal{O}(\delta^{-1})$, where δ is a small parameter of order 10^{-4} (see Table 4.1.1 in Chapter 4 Section 4.1.1). In this limit, the critical values are given by:

$$M_c^2 = \frac{\gamma p}{\gamma p + B^2} \approx 1 - \beta^{-1} \sim 1 - \mathcal{O}(\delta)\,, \tag{6.3}$$

$$M_s^2 = \frac{1}{2}\frac{\gamma p + B^2}{B_p^2}\left(1 - \sqrt{1 - \frac{4\gamma p B_p^2}{(\gamma p + B^2)^2}}\right) \approx M_c^2\left(1 + \beta_p^{-1}\right) \sim M_c^2 + \mathcal{O}\left(\delta^3\right), \tag{6.4}$$

$$M_f^2 = \frac{1}{2}\frac{\gamma p + B^2}{B_p^2}\left(1 + \sqrt{1 - \frac{4\gamma p B_p^2}{(\gamma p + B^2)^2}}\right) \approx \beta_p^{-2} \sim \mathcal{O}\left(\delta^{-3}\right), \tag{6.5}$$

where $\beta_p \equiv \gamma p/B_p^2$.

With this solar ordering, we notice that three of the four critical points appear very close together (see Figure 6.1). To estimate where these critical layers appear in the Sun, we took

the mean poloidal field and flow at the surface and extrapolate downwards along the (nearly axial) flux surfaces that thread the CZ (see Figure 6.2). This gives a value of $M_{AP}^2 \sim 200$ at the surface, decreasing inversely proportional to density, suggesting that the critical layers at $M_{AP}^2 \lesssim 1$ appear at around $\sim 0.7 R_\odot$, suggestively close to the location of the Tachocline.

At the $M_{AP}^2 = 1$ surface, the poloidal projection of propagating Alfvén waves exactly matches the speed of the poloidal flow, and a standing Alfvén shock could appear, producing discontinuities in $\nabla\xi$, $\underline{\mathbf{B}}$, and $\underline{\mathbf{v}}$. These are dissipationless transverse shocks, physically corresponding to an instantaneous rotation of the field and flow about the direction normal to the shock (recall the equation remains elliptic on either side of this surface). Dissipative shocks associated with the hyperbolic layer below the Alfvén surface could also appear.

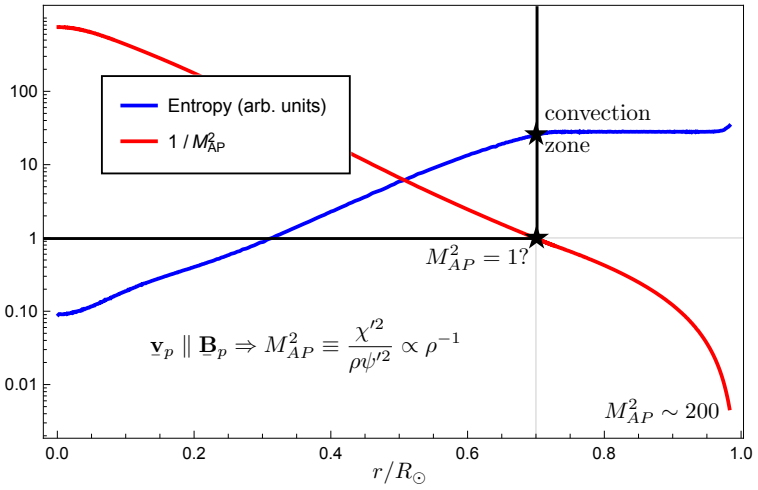

Figure 6.2: **The extrapolated position of the Alfvén surface occurs suggestively close to the base of the Convection Zone.** Using the density and pressure profiles of the standard solar model [44], we plot the entropy as a function of radius (blue curve). Notice that the entropy increases as a function of radius until the onset of convection (around 70% of the solar radius), at which point it is essentially flat. This is essentially the same location as the Tachocline, where the rotation profile changes from uniform to differential. Based on measurements of the solar surface, we assume a surface flow of 15 m s^{-1} and 10^{-3} T at a density of 1 kg m^{-3}. Under the assumption that the flux/stream functions extend from the solar surface to the base of the Convection Zone, M_{AP}^2 is inversely proportional to the density throughout this region (red curve). This resulting putative profile suggests that $M_{AP}^2 \sim 1$ also occurs around the location of the Tachocline.

6.2.1 The roots of the Bernoulli equation

It is not only the PDE (2.18) that must navigate transitions; the algebraic Bernoulli equation (2.17) must choose between different roots. Indeed, as illustrated in Figure 6.3, the derivative of the Bernoulli equation with respect to density has the same sign in both the depths corresponding to the Convection Zone and Radiative Interior (the second and fourth roots of the Bernoulli equation, respectively). However, there should be a brief region in between, just below the Alfvén surface, where this derivative is of the opposite sign.

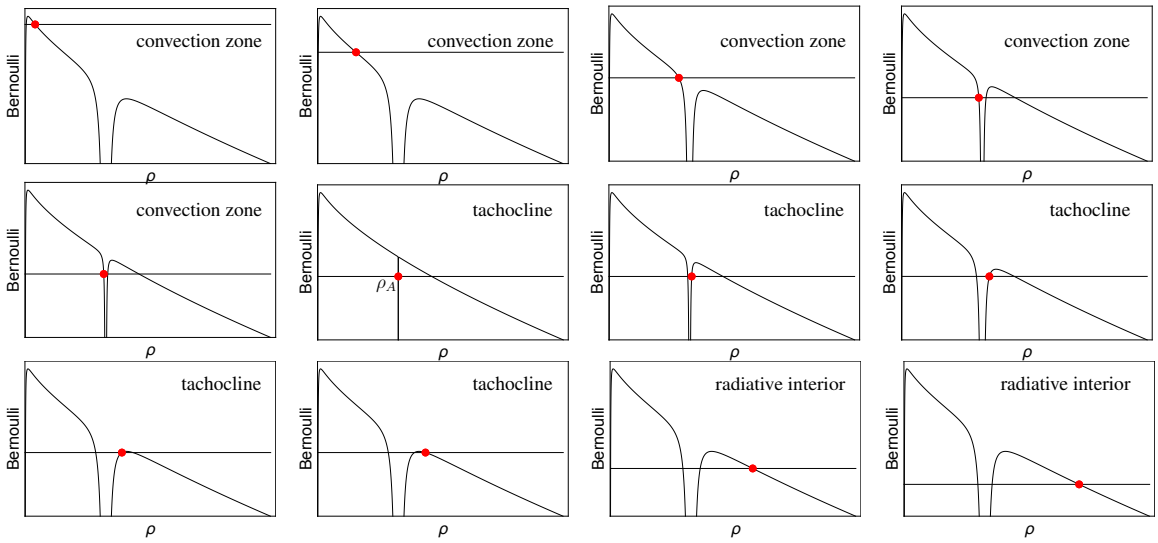

Figure 6.3: **Schematic of smoothly switching between different solutions for the density in the solar relevant regime.**
Here, we consider moving along a single flux/stream surface, starting near the top of the Convection Zone (*upper left*) and ending in the Radiative Interior (*lower right*). The curved lines represent the terms in the Bernoulli equation (2.17) that depend on the density, plotted as a function of density. The remaining terms ($H(\xi)$ and the gravitational potential Φ) are represented by the horizontal lines, and have a value that decreases with depth. Solutions for the Bernoulli equation are given by the intersection of these two curves, and the desired solution is denoted by the red dot.
In general, the Bernoulli equation has either 0, 2 or 4 roots. The smallest root does not occur in our domain, and is indistinguishable from zero in this schematic. The second root is the appropriate choice for the Convection Zone.
As the solution approaches the Alfvén density for this flux/stream surface ($\rho \to \rho_A \equiv \chi'^2/\psi'^2$, ie, $M_{AP}^2 \to 1$), it approaches a "crevasse" (*second row, first frame*), such that the solution seemingly cannot cross to the other side. However, the width of this crevasse is proportional to the difference between the cylindrical radius of this flux/stream surface and its associated Alfvén radius ($\lambda_A \equiv \sqrt{-\psi' L/\chi' F}$). Thus, if the flux/stream surface passes through $\lambda = \lambda_A$, then the second and third solutions coincide at $\rho = \rho_A$ (*second row, second frame*), allowing the solution for the density to smoothly transition between them (*second row, third frame*).
However, the saga of the little red dot is not yet over; it must still find a way out of this crevasse. The horizontal line will continue to decrease, apparently damning our circular friend to the depths of the Alfvénic crevasse. But as the crevasse widens, the barrier to the right is lowered, providing salvation and allowing the solution to smoothly break through to the other side, the fourth root. A more rigorous translation of this story is given in Section 6.4.1.

6.3 Seemingly smooth transitions

We now consider global simulations that contain the aforementioned transitions. In contrast to our strong tachocline hypothesis, in Figure 6.4, we find solar-like equilibria that smoothly cross the Alfvén surface and narrow hyperbolic layer. However, because these transitions occur in a very narrow region ($\sim 10^{-6} R_\odot$), the resolution required to resolve these layers in a global equilibrium is prohibitive.

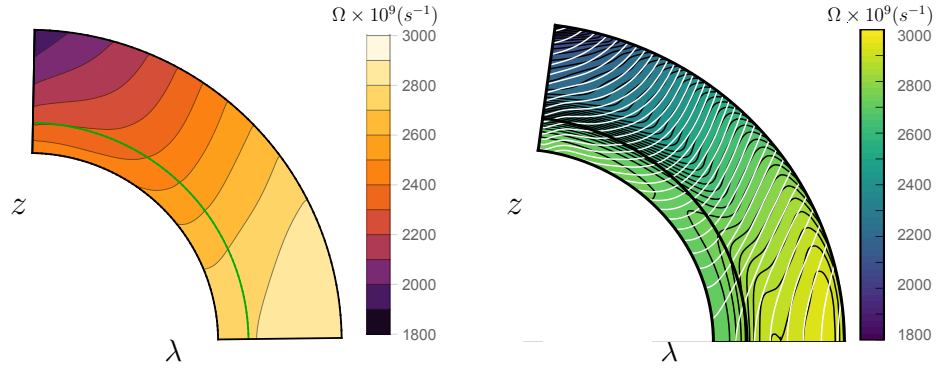

Figure 6.4: **Example of a smooth equilibrium with a "simple" tachocline.** *Left*: We choose the rotation rate to match the solar rotation data from Howe et al. [55] at $r = 0.95 R_\odot$. The parameters controlling the density were chosen such that $\rho = 1$ kg m^{-3} at $r = R_\odot$ and $\rho = 200$ kg m^{-3} at $r = 0.7 R_\odot$, a good approximation to the adiabatic profile in the Convection Zone. The poloidal flow is taken to be 20 m s^{-1} at $r = R_\odot$, approximately equal to the observed poleward poloidal flow on the surface. The entropy gradient was chosen to approximate the tilting of the rotation contours in the Convection Zone. We choose constant $\rho_A \equiv \chi'^2/\psi'^2$, so that the Alfvén surface (denoted by the green line) is essentially spherical. Lastly, we choose the Alfvén radius $\lambda_A \equiv \sqrt{-\psi' L/\chi' F}$ to be equal to the initial cylindrical radius of that flux/stream surface (where it intersects the outer boundary). Thus, the flux/stream surfaces are essentially equally spaced as they cross the Alfvén surface, and do so at nearly the location they would be in hydrodynamic equilibrium. Notice that the physical variables are smooth across the Alfvén surface, in contrast with our strong tachocline hypothesis. However, the layers associated with the transitions are extremely narrow ($\sim 10^{-6} R_\odot$), and are not possible to resolve in such a global simulation; all of the gridpoints are either completely above or below this region. *Right*: Actual solar rotation profile in black (data from [55]), and a profile obtained from the hydrodynamic G–S model in white (see Figure 4.2).

Indeed, it is not uncommon for transitions to be unresolved in global simulations of the G–S equation. For example, Guazzotto et al. [42] left unresolved the small region of hyperbolicity associated with the sonic transition in the tokamak-relevant regime. However, Guazzotto & Hameiri [43] considered a linear 2D model of a two elliptic regions separated by a hyperbolic layer, deriving an exact solution, indicating that treating such problems as an elliptic boundary value problem is in fact well-posed, and can yield smooth solutions. While this small unresolved hyperbolic region may indeed be smooth, it can give rise to discontinuities elsewhere in the equilibrium solution. In fact, such a transition gives rise to the possibility of tokamak equilibria with radial discontinuities in density and poloidal flow.

One particularly tantalizing suggestion is that this strong radial shear could suppress turbulence and serve as an internal transport barrier [41]. This shear is very similar to our desired tachocline result. However, there are a few key differences: the discontinuity studied by Guazzotto & Hameiri is due to the sonic transition, which occurs at a lower velocity in the tokamak-relevant regime; and it is precisely aligned with the flux/stream functions, while our relevant transitions are crossed by the flow. Furthermore, it has been shown that the sonic transition is eliminated in a kinetic treatment due to the effect of Landau damping [15], which is not captured in an MHD model. In contrast, the Alfvén transition persists even in the presence of kinetic effects [15, 57].

Similar to the approach taken by Guazzotto & Hameiri [43], we analyze simplified local models of the transitions to determine if our observed smooth solutions in solar relevant regime are indeed valid equilibria.

6.4 Consistency of the smooth global solutions

6.4.1 1D model for the trans-Alfvénic density profile

We start by analyzing a 1D model representing a single flux/stream surface in order to determine if the density is able to smoothly switch between the three relevant solutions to the Bernoulli equation (see Section 6.2.1, Figure 6.3).

In brief, in the following analysis, we consider the behavior of a single flux/stream surface as a function of depth (as in Figure 6.3). We first neglect the differential terms in both the Bernoulli equation (2.17) and the PDE (2.18). We linearize about the Alfvén surface and show analytically that smooth transitions to the third and fourth roots can indeed occur.

We begin by neglecting the differential terms in the Bernoulli equation (2.17),

$$\frac{1}{2}\frac{\chi'^2}{\rho^2}\left[\left(\frac{L}{\lambda}+\frac{\lambda\chi' F}{\psi'}\right)\Big/\left(\psi'^2-\frac{\chi'^2}{\rho}\right)\right]^2-\frac{1}{2}\frac{\lambda^2F^2}{\psi'^2}+\frac{\gamma}{\gamma-1}\rho^{\gamma-1}e^{\sigma}+\Phi-H(\xi)=0. \quad (6.6)$$

We rewrite this equation in terms of dimensionless quantities as follows:

$$\frac{G}{R_\odot Z}\frac{R_\odot}{r}+\frac{H}{Z}-\frac{\gamma S\rho_A^{\gamma-1}}{(\gamma-1)Z}\left(\frac{\rho}{\rho_A}\right)^{\gamma-1}+\frac{1}{2}\frac{\lambda_A^2}{\lambda^2}\frac{\left(\frac{\lambda^2}{\lambda_A^2}-1\right)^2}{\left(\frac{\rho}{\rho_A}-1\right)^2}-\frac{1}{2}\frac{\lambda^2}{\lambda_A^2}=0, \quad (6.7)$$

where

$$\rho_A \equiv \frac{\chi'^2}{\psi'^2}, \tag{6.8}$$

$$\lambda_A^2 \equiv -\frac{\psi' L}{\chi' F}, \tag{6.9}$$

$$Z \equiv \frac{LF}{\psi'\chi'}, \tag{6.10}$$

$$\Phi \equiv -\frac{G}{r}. \tag{6.11}$$

Likewise, neglecting the differential terms in the PDE (2.18) yields another algebraic expression:

$$\left[\left(\frac{L^2}{2\lambda^2} + \frac{\chi' LF}{\psi'} + \frac{\rho\lambda^2 F^2}{2}\right)\Big/\left(\psi'^2 - \frac{\chi'^2}{\rho}\right) - \frac{1}{\gamma-1}\rho^\gamma e^\sigma + \rho H\right]' = 0, \tag{6.12}$$

which we also write in terms of dimensionless quantities:

$$\begin{aligned}\frac{H'}{Z} - \frac{S'\rho_A^{\gamma-1}}{(\gamma-1)Z}\left(\frac{\rho}{\rho_A}\right)^{\gamma-1} + \frac{1}{2}\frac{\lambda^2}{\lambda_A^2}\Bigg[&\left(\ln(\lambda_A^2)\right)'\frac{\left(\frac{\rho}{\rho_A}-1\right) + \left(\frac{\lambda_A^2}{\lambda^2}-1\right)\left(\frac{\lambda_A^2}{\lambda^2}+1\right)}{\left(\frac{\rho}{\rho_A}-1\right)} \\ &+ \left(\ln(\rho_A)\right)'\frac{\frac{\rho}{\rho_A}\left(\frac{\lambda_A^2}{\lambda^2}-1\right)^2}{\left(\frac{\rho}{\rho_A}-1\right)^2} - \left(\ln(Z)\right)'\frac{\left(\frac{\rho}{\rho_A}-1\right) - \left(\frac{\lambda_A^2}{\lambda^2}-1\right)^2}{\left(\frac{\rho}{\rho_A}-1\right)}\Bigg] = 0.\end{aligned} \tag{6.13}$$

Notice that for both equations (6.7) and (6.13) to be satisfied at the Alfvén surface ($\rho \to \rho_A$), then $\lambda^2 \to \lambda_A^2$ as well. As ρ is nearly spherical, this condition specifies a point in the poloidal plane that a given flux/stream surface must pass through (if it is to cross the Alfvén surface). This essentially "anchors" the flux/stream surface at a specific location

on the Alfvén surface. We consider to the consequences of this anchoring in Section 6.5 (Figure 6.8).

Linear analysis of Alfvén transition

In this linearized regime, we now show that the solution smoothly crosses through all the relevant roots. Precisely, we consider moving along a curve of constant ξ, and evaluate the evolution of the density ρ and cylindrical radius λ as a function of spherical radius r. For fixed ξ, equations (6.7) and (6.13) can be seen as

$$B_{\text{ernoulli}}\big(\tilde{r}, \tilde{\rho}, \tilde{\lambda}^2\big) = 0, \tag{6.14}$$

$$P_{\text{DE}}\big(\tilde{\rho}, \tilde{\lambda}^2\big) = 0, \tag{6.15}$$

where $\tilde{r} \equiv r/R_\odot$, $\tilde{\rho} \equiv \rho/\rho_A$, and $\tilde{\lambda}^2 \equiv \lambda^2/\lambda_A^2$.

To obtain the required slope of the flux/stream surface as it passes through the Alfvén surface, we apply l'Hôpital's rule to the algebraic part of the PDE (6.13):

$$\left.\frac{d(\tilde{\lambda}^2)}{d\tilde{\rho}}\right|_{\tilde{\rho}\to 1, \tilde{\lambda}^2 \to 1} = \frac{\rho_A(\lambda_A^2)'}{\lambda_A^2 \rho_A'} \left\{ 1 \pm \left[1 + \frac{\big(\ln(\rho_A)\big)'}{\big(\ln(\lambda_A^2)\big)'^2} \left(\big(\ln(Z)\big)' - \big(\ln(\lambda_A^2)\big)' + 2\left(\frac{S'\rho_A^{\gamma-1}}{(\gamma-1)Z} - \frac{H'}{Z} \right) \right) \right]^{1/2} \right\}. \tag{6.16}$$

Substituting back into the algebraic part of the Bernoulli equation (6.7), we obtain a second expression to be satisfied at the critical point:

$$\frac{G}{R_\odot Z}\frac{R_\odot}{r} + \frac{H}{Z} - \frac{\gamma S \rho_A^{\gamma-1}}{(\gamma-1)Z} + \frac{1}{2}\frac{\rho_A}{\lambda_A^2}\left(\frac{d(\tilde{\lambda}^2)}{d\tilde{\rho}}\right)_c^2 - \frac{1}{2} = 0. \tag{6.17}$$

This yields an expression for the spherical radius at which the flux/stream surface crosses the Alfvén surface,

$$\tilde{r}_c = -\frac{G}{R_\odot Z}\left(\frac{H}{Z} - \frac{\gamma S \rho_A^{\gamma-1}}{(\gamma-1)Z} + \frac{1}{2}\frac{\rho_A^2}{\lambda_A^4}\frac{\rho_A}{\lambda_A^2}\left(\frac{d(\tilde{\lambda}^2)}{d\tilde{\rho}}\right)_c^2 - \frac{1}{2}\right)^{-1}. \tag{6.18}$$

To obtain the change in density with respect to spherical radius at the Alfvén surface, we substitute into equation (6.7) a linear approximation of $\tilde{\lambda}^2$ as a function of $\tilde{\rho}$:

$$B_{\text{ernoulli}}\left(\tilde{r}, \tilde{\rho}, 1 + \left(\frac{d(\tilde{\lambda}^2)}{d\tilde{\rho}}\right)_c\big(\tilde{\rho} - 1\big)\right) = 0. \tag{6.19}$$

We then differentiate with respect to $\tilde{r}$ and evaluate at the Alfvén point:

$$\frac{\partial B_{\text{ernoulli}}}{\partial \tilde{r}} + \left(\frac{d\tilde{\rho}}{d\tilde{r}}\right)_c\frac{\partial B_{\text{ernoulli}}}{\partial \tilde{\rho}} + \left(\frac{d\tilde{\rho}}{d\tilde{r}}\right)_c\left(\frac{d(\tilde{\lambda}^2)}{d\tilde{\rho}}\right)_c\frac{\partial B_{\text{ernoulli}}}{\partial(\tilde{\lambda}^2)} = 0, \tag{6.20}$$

obtaining

$$\left(\frac{d\tilde{\rho}}{d\tilde{r}}\right)_c = -\frac{\partial B_{\text{ernoulli}}}{\partial \tilde{r}}\Bigg/\left[\frac{\partial B_{\text{ernoulli}}}{\partial \tilde{\rho}} + \left(\frac{d(\tilde{\lambda}^2)}{d\tilde{\rho}}\right)_c\frac{\partial B_{\text{ernoulli}}}{\partial(\tilde{\lambda}^2)}\right]. \tag{6.21}$$

We then substitute this additional linear approximation of $\tilde{\rho}$ as a function of $\tilde{r}$ into equation (6.7):

$$B_{\text{ernoulli}}\left(\tilde{r}, 1 + \left(\frac{d\tilde{\rho}}{d\tilde{r}}\right)_c\big(\tilde{r} - \tilde{r}_c\big), 1 + \left(\frac{d(\tilde{\lambda}^2)}{d\tilde{\rho}}\right)_c\left(\frac{d\tilde{\rho}}{d\tilde{r}}\right)_c\big(\tilde{r} - \tilde{r}_c\big)\right) = \mathcal{O}\big((\tilde{r} - \tilde{r}_c)^2\big). \tag{6.22}$$

Evaluating $\partial B_{\text{ernoulli}}/\partial\tilde{\rho}$ for these linearized parameters, we find that this derivative indeed changes sign in a region just below the Alfvén point (see Figure 6.5 for vizualization). In summary, this analysis suggests that smooth global solutions, despite not resolving the transition layers, are consistent with local solutions that do.

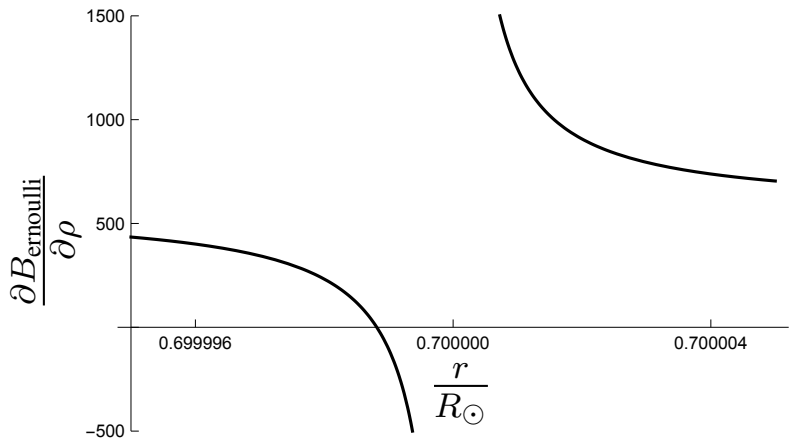

Figure 6.5: **For solar relevant parameters, all the relevant transitions occur in a very narrow region**. We plot $\partial B_{\text{ernoulli}}/\partial\tilde{\rho}$ for the linearized solution (equation (6.22)). In particular, the intermediate solution to the Bernoulli equation (2.17) (characterized by $\partial B_{\text{ernoulli}}/\partial\tilde{\rho} < 0$) is relevant for a narrow region (about $10^{-6}R_\odot$ wide) just below the Alfvén surface at $0.7R_\odot$.

6.4.2 Resolving the transitions in 2D

To corroborate our result from the linear 1D analysis, we use the full set of (nonlinear, 2D) equations (2.18) and (2.17). To this end, we construct a code that automatically zooms in on the region containing the transitions. After many iterations, the resolution is sufficiently high to resolve the layers individually. In Figure 6.6, we plot the derivative of the Bernoulli equation with respect to density, for increasing resolution. The final plot sufficiently resolves the region where this derivative changes sign. As the solutions remain smooth, the smooth global solutions are indeed valid.

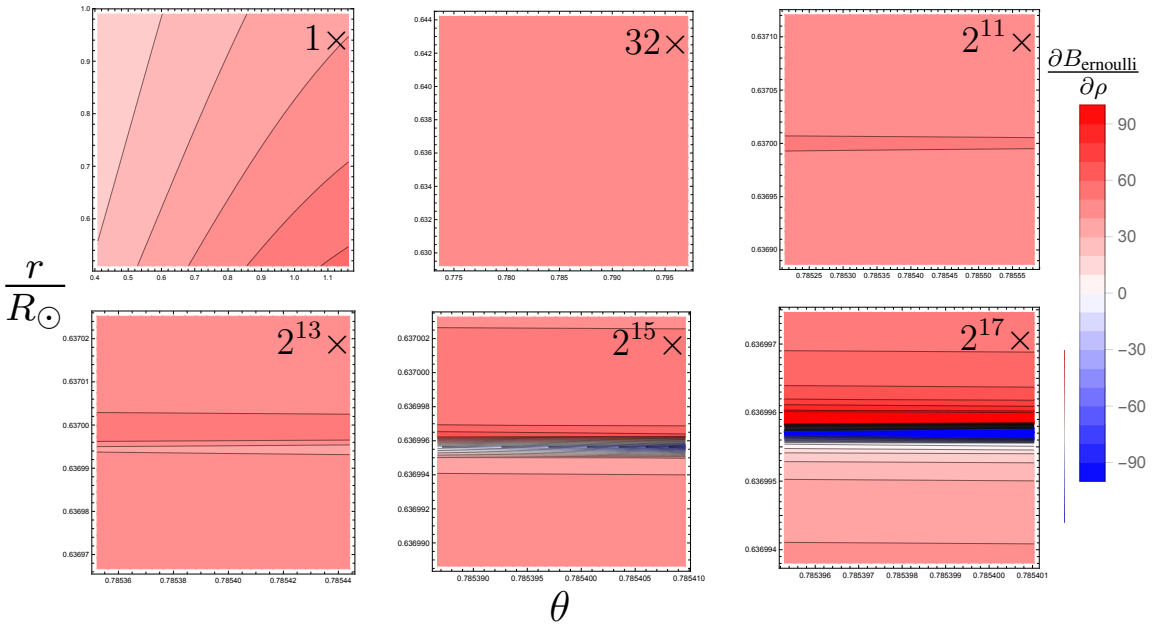

Figure 6.6: **Zooming in on the Alfvén surface confirms the validity of the smooth global solutions**. Our iterative solver automatically approximates the location of the Alfvén surface, zooming in by a factor of 2 each iteration. We plot the derivative of the full Bernoulli equation (2.17) for different resolutions. From the 1D linear analysis (Section 6.4.1), we expect this derivative to briefly change sign just below the Alfvén surface. Indeed, we find the same qualitative behavior for the fully nonlinear 2D PDE. Moreover, the solutions remain smooth, justifying the use of global simulations, which are unable to resolve these layers.

6.5 Perturbing the simple Alfvén surface

Having established that the smooth global solutions are indeed valid, we now further investigate the range of possible smooth solutions. While we have the freedom to choose the six flux/stream functions (Chapter 2 Section 2.3), our knowledge of the Sun constrains some of their profiles. Specifically, the surface poloidal flow constrains χ, and the surface rotation essentially constrains L. The density profile constrains the magnitude of both H and σ, and the tilting of the contours in the Convection Zone constrains $\partial\sigma/\partial\xi$. The arbitrary

choice of labeling the flux/stream surfaces with $\xi \approx \lambda$ at the surface determines $\partial H/\partial \xi$. This leaves unconstrained two flux/stream functions, ψ and F. However, due to the complex and nonlinear relationship between flux/stream functions and the physical variables, we find it more intuitive to represent these degrees of freedom in terms of $\rho_A(\xi)$ (equation (6.8)) and $\lambda_A^2(\xi)$ (equation (6.9)). The former essentially determines the spherical radius of the Alfvén surface, and the latter determines the cylindrical radius at which the flux/stream surfaces will cross the Alfvén surface.

For the previously considered global solution (Figure 6.4), ρ_A was constant, resulting in a nearly spherical Alfvén surface. However, there is evidence that the Tachocline is in fact prolate [19, 25]. In Figure 6.7, we study the effect of changing the shape of the Alfvén surface on the equilibrium profiles. While we find that such manipulations alter the position of the toroidal field, it does not appreciably change the rotation profile.

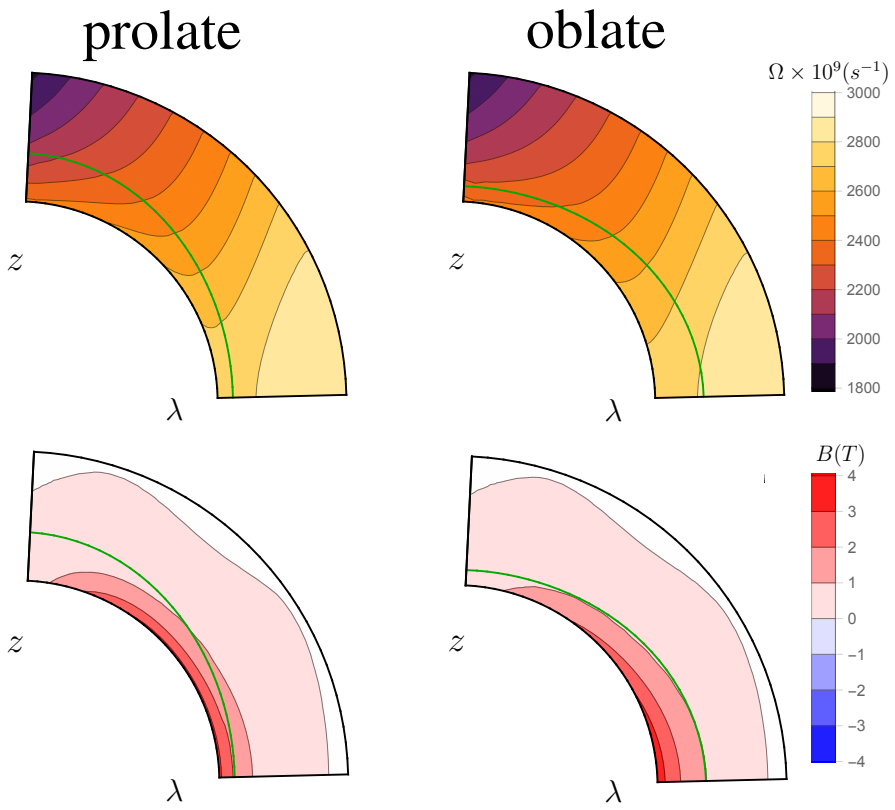

Figure 6.7: **The shape of the Alfvén surface does not appreciably change the rotation profile**. For a constant ratio between χ' and ψ', the Alfvén surface is nearly spherical (see Figure 6.4 left). By allowing this ratio to vary with ξ, we can obtain an Alfvén surface (green curves) with the observed [19, 25] prolateness of the Tachocline (*left images*). For comparison, we also consider equilibria with oblate Alfvén surfaces (*right images*). *Top images* display rotation profiles, and *bottom images* magnetic field profiles. The region of high toroidal field appears to follow the shape of the Alfvén surface. For the rotation, while there is a slight change in the profile (eg, the contours below the Alfvén surface at mid to low latitudes are slightly more curved in the prolate case), there appear to be few fundamental differences.

For the global solutions considered so far, λ_A^2 has been chosen so as to not significantly perturb the poloidal flows from those that would be expected from a hydrodynamic treatment (Figure 6.4). However, in many models of the Sun, the poleward surface flow is considered to return equatorward at the base of the Convection Zone [24]. While recirculating flows

are not compatible with a solar rotation profile under the assumptions of our model (see discussion in Chapter 7 Section 7.2), we can nevertheless construct equilibria with poloidal flows that are suggestive of such flows. In fact, as shown in Figure 6.8, such equilibria display additional solar-like features in their rotation profiles.

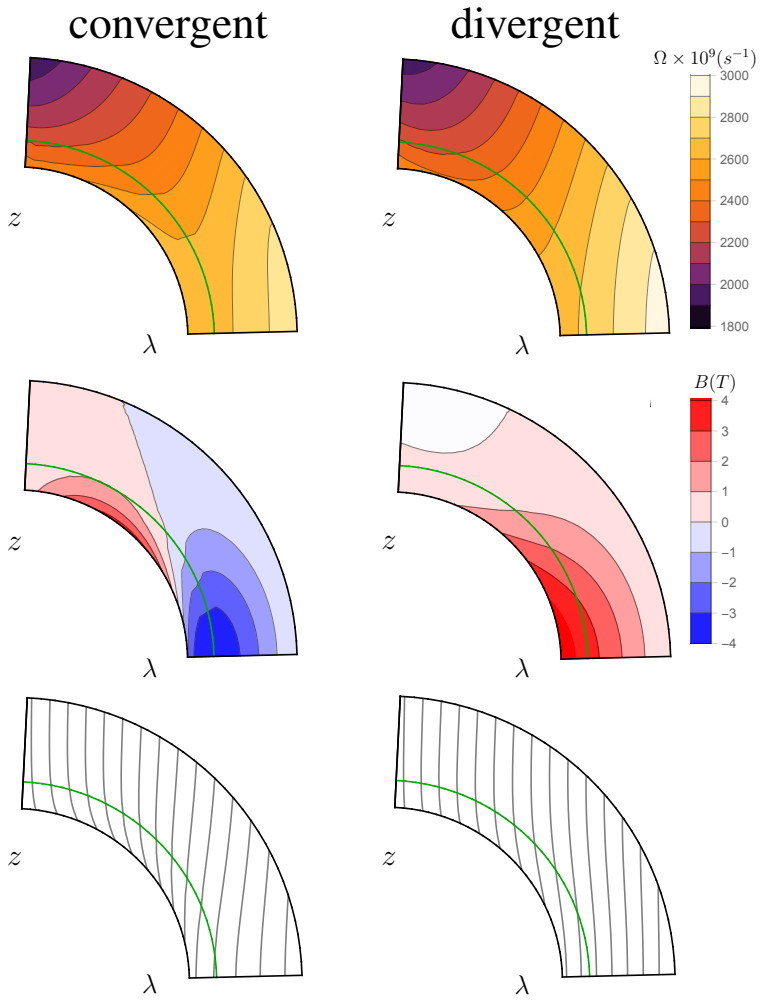

Figure 6.8: **Flux/stream surfaces reminiscent of recirculating flows at the base of the CZ result in more solar-like rotation profiles**. By maintaining a constant ratio between ψ' and χ', we kept the Alfvén surface nearly spherical (as in Figure 6.4, left). While maintaining the same rotation rate at $r = 0.95R_\odot$, we adjusted the profile of the Alfvénic radius λ_A as a function of ξ. The flux/stream surfaces (*bottom images*) are "tethered" to their prescribed cylindrical radii λ_A at the Alfvén surface $\rho = \rho_A$. For the "convergent" case (*left images*), flux/stream surfaces near to the rotation axis have an increased λ_A, while flux/stream surfaces far from the rotation axis have decreased λ_A; they are forced to "converge" towards each other as they approach the Alfvén surface. For the "divergent" case (*right images*), the opposite holds. There is a clear qualitative change in the rotation profile due to this manipulation (*top images*). In particular, the convergent case displays a profile closer to that of the Sun (Figure 6.4, right): rotation contours at the mid to high latitudes display more shear below the Alfvén surface, and the magnetic field displays two bands of opposite sign.

6.6 WKB analysis

Thus far, this chapter has tacitly assumed that the solutions are smooth, without the short wavelength oscillations mentioned in Chapter 5. In this section, we show that, if such oscillations are present in the solution, the linear analysis that was valid for the Convection Zone (Section 5.2) breaks down as one approaches the Alfvén surface.

We first write the PDE (2.18) as:

$$(1-\tilde{\rho})\nabla^2\xi + Q_1(\tilde{\rho},\xi)|\nabla\xi|^2 + Q_2(\tilde{\rho},\xi) = 0. \tag{6.23}$$

Similar to the analysis in Section 5.2, let ξ_0 be a smooth solution to equation (6.23), and consider a perturbed solution $\xi = \xi_0 + \xi_1$. The linearized equation for ξ_1 is approximately

$$(1-\tilde{\rho})\nabla^2\xi_1 + 2Q_1\nabla\xi_0 \cdot \nabla\xi_1 + \left(\frac{\partial Q_2}{\partial \xi}\right)\bigg|_{\xi_0} \xi_1 \approx 0, \tag{6.24}$$

where $(\partial Q_2/\partial\xi)|_{\xi_0}$ is large and positive for $\tilde{\rho} < 1$.

In Chapter 5, we discussed the relevant case for the bulk of the Convection Zone, where the dominant balance given by the first and third terms of equation (6.24), resulting in short wavelength oscillations. As one approaches the Alfvén surface ($\tilde{\rho} \to 1$),

$$\left(\frac{\partial Q_2}{\partial \xi}\right)\bigg|_{\xi_0} \propto \frac{1}{1-\tilde{\rho}}. \tag{6.25}$$

Thus, the wavelength of the oscillatory perturbation decreases proportionally to $1-\tilde{\rho}$.

Let $x = 1-\tilde{\rho}$. Because the density has nearly constant derivative with respect to radius in the region around the Alfvén surface (Section 6.4.1), we treat ξ_1 as a function of x,

arriving at the following approximate expression:

$$\frac{\partial^2 \xi_1}{\partial x^2} + \frac{¢}{x^2}\xi_1 \approx 0, \tag{6.26}$$

where ¢ is a large positive constant. Applying the WKB approximation, we obtain

$$\xi_1 \propto \sqrt{|x|}\exp(i \ln |x|). \tag{6.27}$$

As the oscillations decay in magnitude as one approaches the Alfvén surface, it might appear that we are justified in dropping the second term in equation (6.24). However, care must be taken; as the wavelength of these oscillations also become shorter, the magnitude of the gradient scales as

$$|\nabla \xi_1| \propto \frac{1}{\sqrt{|x|}}. \tag{6.28}$$

Substituting the scaling (6.28) into equation (6.23), we see that the second term grows as $|x|^{-1}$ for $x \to 0$. This is faster than the first and third terms, which both grow as $|x|^{-1/2}$, breaking the Ansatz of dominant balance between these terms near the Alfvén surface. Likewise, the term in the Bernoulli equation containing the spatial derivative of ξ is no longer subdominant. Thus, if such short wavelength oscillations are to exist in the solution, the analysis in Section 6.4 may not be valid; a more delicate treatment of the approach to the Alfvén surface must be performed.

6.7 Discussion: a "weak tachocline hypothesis"

In contrast to our strong tachocline hypothesis, in the absence of oscillatory perturbations, we found solutions that smoothly cross the Alfvén surface (Sections 6.3 and 6.5). However,

while convenient from a mathematical and computational point of view, an absolute absence of short wavelength oscillations is not particularly realistic.

Section 6.2 argues that the Alfvén surface and associated layer of hyperbolicity should occur near the location of the Tachocline. Section 6.6 suggests that even the smallest divergence from the smooth solution necessitates the incorporation of additional physics to explain this region. One might then consider the "weak tachocline hypothesis", positing that localized instabilities associated with these transitions are related to the existence of the Tachocline.

Chapter 7

Prospects

Despair, Hangover & Ecstasy

—— The Dø

7.1 Thesis summary

In this work, we have studied the internal structure of the Sun through the lens of axisymmetric equilibrium MHD with flows. To this end, we developed a code that solves the associated Lagrangian formulation, and applied it to solar-relevant regimes (Chapter 3). In particular, we tested the validity of such an equilibrium description for the four broad regions of the solar interior, namely, Near Surface Shear Layer, Convection Zone, Tachocline, and Radiative Interior.

We find that a purely hydrodynamic equilibrium is sufficient to accurately replicate the observed rotation in the Convection Zone (Chapter 4, Figure 4.2). Moreover, equilibria in this limit exhibit poloidal flows that are aligned with angular momentum, a result corroborated by high-resolution 3D simulations [75]. The inclusion of the poloidal flow implies a slowing

of the rotation at the solar surface, a feature reminiscent of the Near Surface Shear Layer, albeit smaller (Chapter 5, Figure 5.2).

As equilibrium flows are approximately inversely proportional to the density, the poloidal field becomes relatively stronger, and the hydrodynamic limit no longer holds. By extrapolating from the observed surface flows and fields, the poloidal flows are predicted to cross the Alfvénic, slow, and cusp transitions at around 70% of the solar radius, suggestively close to the onset of convection and the notoriously narrow Tachocline (Chapter 6). We find that smooth equilibria crossing these transitions exist, suggesting that axisymmetric equilibrium MHD is unable to produce a tachocline. However, a WKB analysis of perturbations around such equilibria suggests that they may not be generic. Indeed, such transitions are frequently associated with local instabilities and solutions with shocks, and we cannot rule out such possibilities.

7.2 Caveats

One limitation of our model involves the topology of the meridional circulation. Near the surface, poloidal flow becomes radial, which is at odds with reasonable boundary conditions and perpendicular to the observed poleward flow (Figure 6.8, bottom images). Likewise, axially-aligned subsurface flows thread the entire interior and do not exhibit the expected recirculation at the Tachocline or equator. In fact, as angular momentum increases with cylindrical radius everywhere, recirculating flows are incommensurate with solar-like rotation within our model, as they are required to conserve angular momentum.

One possible resolution is that strong convection at the solar surface effectively "rewrites" the flux/stream functions as the flow moves poleward. Likewise, the strongly subadiabatic entropy gradient could serve a similar role at the base of the Convection Zone. The description of such regions would necessarily be outside the scope of the Grad–Shafranov

equilibrium formalism. However, one could envision a model with externally imposed sources and sinks of momentum, magnetic flux, and entropy in these regions that redirect the flow into a recirculating profile. The goal would then be to find physically motivated prescriptions for these external forces that result in plausible solar profiles.

The equator poses a logically parallel (ie, also physically perpendicular) problem; although the Sun exhibits a bipolar magnetic field (particularly during solar minimum, when the equilibrium assumption is most likely to hold), solar flows appear to be predominantly quadripolar. Hence, a global alignment of fields and flows is impossible within the G–S formalism when the equator is within the domain.

7.3 Future directions

7.3.1 Initial conditions for nonlinear simulations

At the end of Chapter 6, we posit a "weak tachocline hypothesis": localized instabilities associated with the transitions near the Alfvén surface are related to the existence of the Tachocline. To properly address this possibility, one would require fully nonlinear 3D simulations (such as the "millennium simulation" discussed in detail by Passos and collaborators [72, 73, 74, 75]). The smooth trans-Alfvénic solutions obtained in Chapter 6 could serve as the initial conditions for such simulations. Seeded by small-amplitude perturbations, the putative local instabilities associated with the transition would grow and interact nonlinearly, and the effects of the resulting turbulence could be quantified. This endeavor could provide insight into dynamic descriptions of the Tachocline, for example: Is the turbulence horizontal, as suggested by Spiegel [90]? If so, does it serve to homogenize the rotation in the interior, or does it do the opposite, as suggested by Rogers et al. [81]? What is the relative importance of the gravity waves excited by solar convection?

The solar-relevant equilibria presented in this work contain several transitions in a narrow region surrounding the Alfvén surface, and suggest that these occur close to the base of Convection Zone. In addition to the variations in the parameters considered in Figures 6.7 and 6.8, such simulations could assess the importance of the *relative* position of the onset of convection with respect to these transitions [103].

7.3.2 Solar cycle

As torsional oscillations are synchronized with the solar cycle, their descriptions are clearly intertwined [65]. While the timescale of the solar cycle ($\sim$11 years) sits comfortably above those of convective turbulence ($\lesssim$1 month), the relaxation time associated with the axisymmetric MHD equilibria are notably longer. For example, the poloidal flow circulates on a timescale comparable to the solar cycle, so the equilibration of angular momentum must be at least as long. Nevertheless, it is not unreasonable (and potentially insightful, see Chapter 2 Section 2.1) to ask: are torsional oscillations necessarily dynamic in nature, or could they be described by a series of quasi-static solar equilibria?

7.3.3 Applications to other systems

Other stars

Potentially fruitful applications of this equilibrium framework extend beyond the Sun's gravitational influence. For example, spectropolarimetry offers information about the surface magnetic fields of other stars, and the developing field of asteroseismology can probe their interior structure [34, 31]. Such "multi-stellar" data could be used both to inform and validate such an equilibrium model.

Gas giants

The Juno mission [1] could provide another astrophysical dataset of particular interest. The mission is currently collecting data about Jupiter's magnetic and gravitational fields [5], and there are many open questions about its interior structure [100]. For example: are the zonal flows confined close to the surface, or do they extend deeper, forming columnar structures as the Taylor–Proudman theorem would suggest? Much like the solar case, the partial information obtained from observations would constrain the choice of flux/stream functions, and solutions to the generalized G–S equation could provide plausible equilibrium models of the Jovian interior.

Magnetoelectric confinement

Terrestrially, a particularly promising application is the modeling of magnetoelectric confinement experiments, such as rotating tori. These toroidal devices do not rely on rotational transform of the magnetic field [56, 76]; instead, the vertical drift is averaged via a strong poloidal flow [93]. In contrast to typical tokamak configurations, the poloidal Alfvénic Mach number in these experiments can easily exceed unity [69], and an Alfvén surface could appear. Through proper modeling of this transition, one might gain additional control over the internal profile and transport properties in such devices.

Bibliography

[1] https://www.nasa.gov/mission_pages/juno.

[2] De laval. US Patent 522,066, Jun 26 1894.

[3] ACEVEDO-ARREGUIN, L. A., GARAUD, P., AND WOOD, T. S. Dynamics of the solar tachocline - iii. numerical solutions of the gough and mcintyre model. *Monthly Notices of the Royal Astronomical Society 434*, 1 (2013), 720–741.

[4] BABCOCK, H. The topology of the sun's magnetic field and the 22-year cycle. *The Astrophysical Journal 133* (1961), 572.

[5] BAGENAL, F., ADRIANI, A., ALLEGRINI, F., BOLTON, S., BONFOND, B., BUNCE, E., CONNERNEY, J., COWLEY, S., EBERT, R., GLADSTONE, G., ET AL. Magnetospheric science objectives of the juno mission. *Space Science Reviews 213*, 1-4 (2017), 219–287.

[6] BALBUS, S. A. A simple model for solar isorotational contours. *Monthly Notices of the Royal Astronomical Society 395*, 4 (2009), 2056–2064.

[7] BALBUS, S. A., BONART, J., LATTER, H. N., AND WEISS, N. O. Differential rotation and convection in the sun. *Monthly Notices of the Royal Astronomical Society 400*, 1 (2009), 176–182.

[8] BALBUS, S. A., AND LATTER, H. N. The tachocline and differential rotation in the sun. *Monthly Notices of the Royal Astronomical Society 407*, 4 (2010), 2565–2574.

[9] BALBUS, S. A., LATTER, H. N., AND WEISS, N. O. Global model of differential rotation in the sun. *Monthly Notices of the Royal Astronomical Society 420*, 3 (2012), 2457–2466.

[10] BALBUS, S. A., AND SCHAAN, E. The stability of stratified, rotating systems and the generation of vorticity in the sun. *Monthly Notices of the Royal Astronomical Society 426*, 2 (2012), 1546–1557.

[11] BARNABÉ, R., STRUGAREK, A., CHARBONNEAU, P., BRUN, A. S., AND ZAHN, J.-P. Confinement of the solar tachocline by a cyclic dynamo magnetic field. *Astronomy & Astrophysics 601* (2017).

[12] BEAUDOIN, P., CHARBONNEAU, P., RACINE, E., AND SMOLARKIEWICZ, P. K. Torsional oscillations in a global solar dynamo. *Solar Physics 282*, 2 (2013), 335–360.

[13] BERRES, S., BURGER, R., AND KOZAKEVICIUS, A. Numerical approximation of oscillatory solutions of hyperbolic-elliptic systems of conservation laws by multiresolution schemes. *Advances in Applied Mathematics and Mechanics 1*, 5 (2009), 581–614.

[14] BESKIN, V. S. Grad-shafranov approach to axisymmetric stationary flows in astrophysics. *JKPS 45* (2004), 1711–1718.

[15] BHATTACHARJEE, A. Mhd equilibrium and stability of axisymmetric plasmas in the presence of rotation. *Technical Report* (1987).

[16] BUSSE, F. Convective flows in rapidly rotating spheres and their dynamo action. *Physics of Fluids 14*, 4 (2002), 1301–1314.

[17] CARRINGTON, R. On two cases of solar spots in high latitudes, and on the surface currents indicated by the observations. *Monthly Notices of the Royal Astronomical Society 20* (1860), 254.

[18] CHARBONNEAU, P. Dynamo models of the solar cycle. *Living Reviews in Solar Physics 7*, 1 (2010), 3.

[19] CHARBONNEAU, P., CHRISTENSEN-DALSGAARD, J., HENNING, R., LARSEN, R. M., SCHOU, J., THOMPSON, M. J., AND TOMCZYK, S. Helioseismic constraints on the structure of the solar tachocline. *The Astrophysical Journal 527*, 1 (1999), 445.

[20] CHAZELLE, B. *The Discrepancy Method: Randomness and Complexity*. Cambridge University Press, 2000.

[21] CHOUDHURI, A. R., SCHUSSLER, M., AND DIKPATI, M. The solar dynamo with meridional circulation. *Astronomy & Astrophysics 303* (1995), L29.

[22] CHRISTENSEN-DALSGAARD, J., DÄPPEN, W., AJUKOV, S., ANDERSON, E., ANTIA, H., BASU, S., BATURIN, V., BERTHOMIEU, G., CHABOYER, B., CHITRE, S., ET AL. The current state of solar modeling. *Science 272*, 5266 (1996), 1286–1292.

[23] CREW, H. On the period of the rotation of the sun as determined by the spectroscope. *American Journal of Science*, 206 (1888), 151–159.

[24] DIKPATI, M., AND CHARBONNEAU, P. A babcock-leighton flux transport dynamo with solar-like differential rotation. *The Astrophysical Journal 518*, 1 (1999), 508.

[25] DIKPATI, M., AND GILMAN, P. A. Prolateness of the solar tachocline inferred from latitudinal force balance in a magnetohydrodynamic shallow-water model. *The Astrophysical Journal 552*, 1 (2001), 348.

[26] DZIEMBOWSKI, W., GOODE, P. R., AND LIBBRECHT, K. The radial gradient in the sun's rotation. *The Astrophysical Journal 337* (1989), L53–L57.

[27] FEATHERSTONE, N. A., AND MIESCH, M. S. Meridional circulation in solar and stellar convection zones. *The Astrophysical Journal 804*, 1 (2015), 67.

[28] FERRARO, V. C. The non-uniform rotation of the sun and its magnetic field. *Monthly Notices of the Royal Astronomical Society 97* (1937), 458.

[29] FIX, G. J., AND GURTIN, M. E. On patched variational principles with application to elliptic and mixed elliptic-hyperbolic problems. *Numerische Mathematik 28*, 3 (1977), 259–271.

[30] FOUKAL, P. Magnetic coupling of the active chromosphere to the solar interior. *The Astrophysical Journal 173* (1972), 439.

[31] FULLER, J., CANTIELLO, M., STELLO, D., GARCIA, R. A., AND BILDSTEN, L. Asteroseismology can reveal strong internal magnetic fields in red giant stars. *Science 350*, 6259 (2015), 423–426.

[32] GASTINE, T., YADAV, R., MORIN, J., REINERS, A., AND WICHT, J. From solar-like to antisolar differential rotation in cool stars. *Monthly Notices of the Royal Astronomical Society: Letters 438*, 1 (2013), L76–L80.

[33] GEUZAINE, C., AND REMACLE, J.-F. Gmsh: A 3-d finite element mesh generator with built-in pre-and post-processing facilities. *IJNME 79*, 11 (2009), 1309–1331.

[34] GILLILAND, R. L., BROWN, T. M., CHRISTENSEN-DALSGAARD, J., KJELDSEN, H., AERTS, C., APPOURCHAUX, T., BASU, S., BEDDING, T. R., CHAPLIN, W. J., CUNHA, M. S., ET AL. Kepler asteroseismology program: introduction and first results. *Publications of the Astronomical Society of the Pacific 122*, 888 (2010), 131.

[35] GILMAN, P. A., AND MIESCH, M. S. Limits to penetration of meridional circulation below the solar convection zone. *The Astrophysical Journal 611*, 1 (2004), 568.

[36] GOEDBLOED, J. P., BELIËN, A. J. C., VAN DER HOLST, B., AND KEPPENS, R. Unstable continuous spectra of transonic axisymmetric plasmas. *Physics of Plasmas 11*, 1 (2004), 28–54.

[37] GOEDBLOED, J. P., AND LIFSCHITZ, A. Stationary symmetric magnetohydrodynamic flows. *Physics of Plasmas 4*, 10 (1997), 3544–3564.

[38] GOUGH, D. Our first inferences from helioseismology. *Physics Bulletin 34*, 12 (1983), 502.

[39] GOUGH, D. O., AND MCINTYRE, M. E. Inevitability of a magnetic field in the sun's radiative interior. *Nature 394*, 6695 (1998), 755–757.

[40] GRAD, H., AND RUBIN, H. Hydromagnetic equilibria and force-free fields. *JNuE 7*, 3-4 (1958), 284–285.

[41] GUAZZOTTO, L., AND BETTI, R. Magnetohydrodynamic mechanism for pedestal formation. *Physical Review Letters 107*, 12 (2011), 125002.

[42] GUAZZOTTO, L., BETTI, R., MANICKAM, J., AND KAYE, S. Numerical study of tokamak equilibria with arbitrary flow. *Physics of Plasmas 11*, 2 (2004), 604–614.

[43] GUAZZOTTO, L., AND HAMEIRI, E. A model for transonic plasma flow. *Physics of Plasmas 21*, 2 (2014), 022512.

[44] GUENTHER, D., DEMARQUE, P., KIM, Y.-C., AND PINSONNEAULT, M. Standard solar model. *The Astrophysical Journal 387* (1992), 372–393.

[45] GUERRERO, G., SMOLARKIEWICZ, P. K., DAL PINO, E. M. D. G., KOSOVICHEV, A. G., AND MANSOUR, N. N. Understanding solar torsional oscillations from global dynamo models. *The Astrophysical Journal Letters 828*, 1 (2016), L3.

[46] GUNDERSON, L., AND BHATTACHARJEE, A. A model of solar equilibrium: the hydrodynamic limit. *The Astrophysical Journal 870*, 1 (2019), 47.

[47] HALE, G. E. On the probable existence of a magnetic field in sun-spots. *The Astrophysical Journal 28* (1908), 315.

[48] HAMEIRI, E. The equilibrium and stability of rotating plasmas. *Physics of Fluids 26*, 1 (1983), 230–237.

[49] HANASOGE, S. M., DUVALL, T. L., AND SREENIVASAN, K. R. Anomalously weak solar convection. *Proceedings of the National Academy of Sciences 109*, 30 (2012), 11928–11932.

[50] HANSEN, C. J., KAWALER, S. D., AND TRIMBLE, V. *Stellar interiors: physical principles, structure, and evolution*. Springer Science & Business Media, 2012.

[51] HATHAWAY, D. H. The solar cycle. *Living Reviews in Solar Physics 12*, 1 (2015), 1–87.

[52] HAZELTINE, R. D., LEE, E. P., AND ROSENBLUTH, M. Rotation of tokamak equilibria. *Physical Review Letters 25*, 7 (1970), 427.

[53] HEINEMANN, M., AND OLBERT, S. Axisymmetric ideal mhd stellar wind flow. *Journal of Geophysical Research 83*, A6 (1978), 2457–2460.

[54] HOTTA, H., REMPEL, M., AND YOKOYAMA, T. High-resolution calculation of the solar global convection with the reduced speed of sound technique. ii. near surface shear layer with the rotation. *The Astrophysical Journal 798*, 1 (2014), 51.

[55] HOWE, R., LARSON, T. P., SCHOU, J., HILL, F., KOMM, R., CHRISTENSEN-DALSGAARD, J., AND THOMPSON, M. J. First global rotation inversions of HMI data. In *J. Phys.: Conf. Ser.* (Jan. 2011), vol. 271 of *Journal of Physics Conference Series*, p. 012061.

[56] HUDSON, S., ZHU, C., PFEFFERLÉ, D., AND GUNDERSON, L. Differentiating the shape of stellarator coils with respect to the plasma boundary. *Physics Letters A 382*, 38 (2018), 2732–2737.

[57] IACONO, R., BONDESON, A., TROYON, F., AND GRUBER, R. Axisymmetric toroidal equilibrium with flow and anisotropic pressure. *Physics of Fluids B: Plasma Physics 2*, 8 (1990), 1794–1803.

[58] KEPPENS, R., AND GOEDBLOED, J. Numerical simulations of stellar winds: polytropic models. *Astronomy & Astrophysics 343* (1999), 251–260.

[59] KITCHATINOV, L. L., AND RÜDIGER, G. Differential rotation in solar-type stars: revisiting the taylor-number puzzle. *Astronomy and Astrophysics 299* (1995), 446.

[60] LANDER, S. K. Magnetic fields in superconducting neutron stars. *Physical Review Letters 110*, 7 (2013), 071101.

[61] LANDER, S. K., AND JONES, D. I. Magnetic fields in axisymmetric neutron stars. *Monthly Notices of the Royal Astronomical Society 395*, 4 (2009), 2162–2176.

[62] LANTZ, S., AND FAN, Y. Anelastic magnetohydrodynamic equations for modeling solar and stellar convection zones. *The Astrophysical Journal Supplement Series 121*, 1 (1999), 247.

[63] LOVELACE, R., MEHANIAN, C., MOBARRY, C., AND SULKANEN, M. Theory of axisymmetric magnetohydrodynamic flows-disks. *The Astrophysical Journal Supplement Series 62* (1986), 1–37.

[64] MCINTYRE, M. E. Solar tachocline dynamics: eddy viscosity, anti-friction, or something in between. *Stellar Astrophysical Fluid Dynamics (ed. MJ Thompson & J. Christensen-Dalsgaard)* (2003), 111–130.

[65] MIESCH, M. S. Large-scale dynamics of the convection zone and tachocline. *Living Reviews in Solar Physics 2*, 1 (2005), 11.

[66] MIESCH, M. S., BRUN, A. S., AND TOOMRE, J. Solar differential rotation influenced by latitudinal entropy variations in the tachocline. *The Astrophysical Journal 641*, 1 (2006), 618.

[67] MIESCH, M. S., FEATHERSTONE, N. A., REMPEL, M., AND TRAMPEDACH, R. On the amplitude of convective velocities in the deep solar interior. *The Astrophysical Journal 757*, 2 (2012), 128.

[68] MIESCH, M. S., AND HINDMAN, B. W. Gyroscopic pumping in the solar near-surface shear layer. *The Astrophysical Journal 743*, 1 (2011), 79.

[69] OCHS, I., AND FISCH, N. Particle orbits in a force-balanced, wave-driven, rotating torus. *Physics of Plasmas 24*, 9 (2017), 092513.

[70] OKAMOTO, I. Magnetic braking by a stellar wind- v approximate determination of the poloidal field. *Monthly Notices of the Royal Astronomical Society 173*, 2 (1975), 357–379.

[71] PARKER, E. N. Dynamics of the interplanetary gas and magnetic fields. *The Astrophysical Journal 128* (1958), 664.

[72] PASSOS, D., AND CHARBONNEAU, P. Characteristics of magnetic solar-like cycles in a 3d mhd simulation of solar convection. *Astronomy & Astrophysics 568* (2014), A113.

[73] PASSOS, D., CHARBONNEAU, P., AND MIESCH, M. Meridional circulation dynamics from 3d magnetohydrodynamic global simulations of solar convection. *The Astrophysical Journal Letters 800*, 1 (2015), L18.

[74] PASSOS, D., CHARBONNEAU, P., AND MIESCH, M. S. New insights about meridional circulation dynamics from 3d mhd global simulations of solar convection and dynamo action. *Coimbra Solar Physics Meeting 504* (2016), 179.

[75] PASSOS, D., MIESCH, M. S., GUERRERO, G., AND CHARBONNEAU, P. Meridional circulation dynamics in a cyclic convective dynamo. *Astronomy & Astrophysics* (2017).

[76] PFEFFERLÉ, D., GUNDERSON, L., HUDSON, S. R., AND NOAKES, L. Non-planar elasticae as optimal curves for the magnetic axis of stellarators. *Physics of Plasmas 25*, 9 (2018), 092508.

[77] RAJAGURU, S. P., AND ANTIA, H. M. Meridional circulation in the solar convection zone: time-distance helioseismic inferences from four years of hmi/sdo observations. *The Astrophysical Journal 813*, 2 (2015), 114.

[78] REMPEL, M. Solar differential rotation and meridional flow: the role of a subadiabatic tachocline for the taylor-proudman balance. *The Astrophysical Journal 622*, 2 (2005), 1320.

[79] REMPEL, M. Origin of solar torsional oscillations. *The Astrophysical Journal 655*, 1 (2007), 651.

[80] ROACH, J. Astrophysicist recognized for discovery of solar wind. *National Geographic News 27* (2003).

[81] ROGERS, T., MACGREGOR, K., AND GLATZMAIER, G. Non-linear dynamics of gravity wave driven flows in the solar radiative interior. *Monthly Notices of the Royal Astronomical Society 387*, 2 (2008), 616–630.

[82] ROSENCRANS, S. On schwarzschild's criterion. *SIAM Journal on Applied Mathematics 17*, 2 (1969), 231–239.

[83] ROSSO, F., AND PELLETIER, G. A variational method for solving fast mhd flows. consequences for stellar and extragalactic jets. *Astronomy & Astrophysics 287* (1994), 325–337.

[84] RÜDIGER, G., AND KITCHATINOV, L. L. The slender solar tachocline: a magnetic model. *Astronomische Nachrichten 318*, 5 (1997), 273–279.

[85] RÜDIGER, G., AND KITCHATINOV, L. L. Structure and stability of the magnetic solar tachocline. *New Journal of Physics 9*, 8 (2007), 302.

[86] SAKURAI, T. Magnetic stellar winds-a 2-d generalization of the weber-davis model. *Astronomy and Astrophysics 152* (1985), 121–129.

[87] SCHWABE, H., AND SCHWABE, H. Sonnen—beobachtungen im jahre 1843. *Astronomische Nachrichten 21*, 15 (1844), 234–235.

[88] SONNERUP, B. U. Ö., HASEGAWA, H., TEH, W.-L., AND HAU, L.-N. Grad-shafranov reconstruction: An overview. *Journal of Geophysical Research 111*, A9 (2006), A09204.

[89] SPIEGEL, E. A. *A History of Solar Rotation*, vol. 300. NASA Special Publication, 1972, p. 61.

[90] SPIEGEL, E. A., AND ZAHN, J.-P. The solar tachocline. *Astronomy & Astrophysics 265* (1992), 106–114.

[91] STEIN, S., AND WYSESSION, M. *An introduction to seismology, earthquakes, and earth structure*. John Wiley & Sons, 2009.

[92] STEINHAUER, L. C. Formalism for multi-fluid equilibria with flow. *Physics of Plasmas 6*, 7 (1999), 2734–2741.

[93] STIX, T. H. Some toroidal equilibria for plasma under magnetoelectric confinement. *Physics of Fluids 14*, 3 (1971), 692–701.

[94] TALON, S., KUMAR, P., AND ZAHN, J.-P. Angular momentum extraction by gravity waves in the sun. *The Astrophysical Journal Letters 574*, 2 (2002), L175.

[95] THOMPSON, M. A new inversion of solar rotational splitting data. *Solar Physics 125*, 1 (1990), 1–12.

[96] THROUMOULOPOULOS, G., AND PANTIS, G. Analytic axisymmetric magnetohydrodynamic equilibria of a plasma torus with toroidal mass flow. *Physics of Fluids B: Plasma Physics 1*, 9 (1989), 1827–1833.

[97] VORONTSOV, S. V., CHRISTENSEN-DALSGAARD, J., SCHOU, J., STRAKHOV, V. N., AND THOMPSON, M. J. Helioseismic measurement of solar torsional oscillations. *Science 296*, 5565 (2002), 101–103.

[98] WEBER, E. J., AND DAVIS JR, L. The angular momentum of the solar wind. *The Astrophysical Journal 148* (1967), 217–227.

[99] WEISSKOPF, V. F. Development of field theory in the last 50 years. *Physics Today 34*, 11 (1981), 69–85.

[100] WICHT, J., GASTINE, T., DUARTE, L. D., AND DIETRICH, W. Dynamo action of jupiter's zonal winds. *Astronomy & Astrophysics 629* (2019), A125.

[101] WILCOX, J. M., AND HOWARD, R. Differential rotation of the photospheric magnetic field. *Solar Physics 13*, 2 (1970), 251–260.

[102] WILLIS, D. M., AND STEPHENSON, F. R. Solar and auroral evidence for an intense recurrent geomagnetic storm during december in ad 1128. *Annales Geophysicae 19* (2001).

[103] WOOD, T. *The solar tachocline: a self-consistent model of magnetic confinement*. PhD thesis, University of Cambridge, 2011.

[104] WOOD, T. S., MCCASLIN, J. O., AND GARAUD, P. The sun's meridional circulation and interior magnetic field. *The Astrophysical Journal 738*, 1 (2011), 47.

[105] WOOD, T. S., AND MCINTYRE, M. E. Polar confinement of the sun's interior magnetic field by laminar magnetostrophic flow. *Journal of Fluid Mechanics 677* (2011), 445–482.

[106] WOOLLEY, R. Convection in the outer layers of the sun. *Monthly Notices of the Royal Astronomical Society 101* (1941), 52.

[107] ZHAO, J., BOGART, R. S., KOSOVICHEV, A. G., DUVALL JR, T. L., AND HARTLEP, T. Detection of equatorward meridional flow and evidence of double-cell meridional circulation inside the sun. *The Astrophysical Journal Letters 774*, 2 (2013), L29.

[108] ZHEN-TAO, X. The hexagram "feng" in "the book of changes" as the earliest written record of sunspot. *Chinese Astronomy 4*, 4 (1980), 406.